A ratchet-like apical constriction drives cell ingression during the mouse gastrulation EMT

Alexandre Francou, Kathryn V. Anderson[#], Anna-Katerina Hadjantonakis*

Developmental Biology Program, Sloan Kettering Institute, Memorial Sloan Kettering Cancer Center, New York, NY 10065, USA

*Correspondence: hadj@mskcc.org

[#]Deceased

ABSTRACT

Epithelial-to-Mesenchymal Transition (EMT) is a fundamental process in which epithelial cells acquire mesenchymal phenotypes and the ability to migrate. EMT is the hallmark of gastrulation, an evolutionarily conserved developmental process. In mammals, epiblast cells lose pluripotency and ingress at the primitive streak to form mesoderm. Cell exit from the epiblast epithelial layer and the associated EMT are dynamically regulated processes involving a stereotypical sequence of cell behaviors. 3D time-lapse imaging of gastrulating mouse embryos combined with cell and tissue scale data analyses revealed the stochastic-like ingression of epiblast cells at the primitive streak. Ingressing cells constrict their apical surfaces in a pulsed ratchet-like fashion through asynchronous shrinkage of apical junctions. A quantitative analyses of the distribution of apical proteins, revealed the anisotropic and complementary distribution of members of the actomyosin network and Crumbs2 complexes, potential regulators of asynchronous shrinkage of cell junctions. The analysis of mutants demonstrated a requirement for Crumbs2 in Myosin2 localization and activity at apical junctions, and as a candidate for regulating actomyosin anisotropy.

INTRODUCTION

Epithelial-to-Mesenchymal Transitions (EMTs) are morphogenetic programs necessary for the formation of tissues throughout embryonic development, cancer progression and metastasis (Francou and Anderson, 2020; Thiery, 2002; Thiery et al., 2009; Ye and Weinberg, 2015). The EMT that occurs during embryo gastrulation is an evolutionarily conserved event occurring in triploblasts as they form three definitive germ layers (Lim and Thiery, 2012; Nakaya and Sheng, 2008; Thiery et al., 2009).

In amniotes the onset of gastrulation involves formation of the primitive streak at the posterior epiblast, at around embryonic **(E)** 6.5 day in the mouse (Ferrer-Vaquer et al.,

2010; Nakaya and Sheng, 2008; Williams et al., 2012) (Figure 1A). Primitive streak initiation is regulated by the convergence of WNT, BMP and Nodal signals, which together with an FGF input trigger the EMT process (Ferrer-Vaquer et al., 2010; Morgani and Hadjantonakis, 2020; Ramkumar and Anderson, 2011). The basement membrane is broken down at the primitive streak facilitating movement of cells out of the epiblast tissue layer, accompanied by changes in their cell shape, including apical constriction and basal translocation of cell bodies (Ramkumar et al., 2016; Williams et al., 2012). Basal cell ingression and migration away from the epiblast epithelium is facilitated though the dissolution of apical junctions. As cells at the primitive streak undergo EMT, more laterally positioned epiblast cells converge toward the midline (Williams et al., 2012), replenishing the pool for continued ingression and ensuring epithelial integrity.

Apical constriction is an epithelial cell shape change associated with morphogenetic processes such as tissue bending, cell delamination and internalization (An et al., 2017; Chung et al., 2017; Lecuit and Lenne, 2007; Martin and Goldstein, 2014; Nishimura et al., 2012; Samarage et al., 2015; Simoes et al., 2017). The dynamics of apical constriction at gastrulation have been studied in invertebrates, particularly in Drosophila, and shown to be controlled by apical actomyosin contractility (Marston et al., 2016; Martin and Goldstein, 2014; Martin et al., 2009; Mason et al., 2013; Roh-Johnson et al., 2012). Apical constriction has been associated with cell ingression during the gastrulation EMT in chick and mouse (Rozbicki et al., 2015; Serrano Najera and Weijer, 2020; Williams et al., 2012), but how cells dynamically constrict apical surfaces during EMT, and what regulates this process remain open questions. Gastrulation process in Drosophila and mouse cannot be directly compared as they exhibit major different time-scales (20min vs. >24hr days), mechanisms and spatial parameters (tissue invagination vs. cell ingression). In the chick embryo, Myosin-2 plays a role in the formation of the primitive streak and cell ingression from the epiblast layer (Chuai et al., 2006; Rozbicki et al., 2015; Serrano Najera and Weijer, 2020; Voiculescu et al., 2007; Voiculescu et al., 2014). Crumbs2, a protein shown to regulate apical polarity in epithelia, is critical for cell ingression during gastrulation EMT in mouse embryos (Ramkumar et al., 2016). Apical Crumbs2 and Myosin-2B show an anisotropic accumulation in mouse epiblast cells in the vicinity of the primitive streak

(Ramkumar et al., 2016), reminiscent of patterns controlling apical constriction during Drosophila salivary gland development (Roper, 2012), suggesting these proteins are potential regulators of apical constriction during mouse EMT. Visualizing the cellular dynamics of the epiblast during mouse gastrulation has been a longstanding challenge due to its internal location which limits optical access and visualization at high resolution.

Using live imaging of *ex utero* cultured mouse embryos, and high resolution visualization and segmentation of epiblast cell membranes, we performed a dynamic quantitative analysis of apical constriction associated with ingression during the mouse gastrulation EMT. We observed cells undergoing EMT at the mouse primitive streak in a stochastic-like manner, constricting their apical surfaces in a rachet-like pulsed fashion through asynchronous shrinkage of apical cell-cell junctions. By analyzing and quantifying the distribution of apical proteins, we uncovered the anisotropic and complementary distribution of actomyosin network and Crumbs complex proteins consistent with a role in regulating junctional shrinkage and apical constriction. The localization of the apical actomyosin network, as well as two kinases aPKC and Rock1, was perturbed in *Crumbs2* mutants, thereby identifying key components of a putative regulatory network driving apical constriction.

RESULTS

Epiblast cells undergo apical constriction and isolated ingression at the mouse primitive streak

The mouse gastrulation EMT occurs at the primitive streak, which, by contrast to the chick, does not form a morphologically distinct domain (Figure 1A,B). Columnar epithelial epiblast cells with their apical surfaces facing the inner (amniotic) cavity of the embryo apically constrict and elongate basally as they ingress out of the epiblast layer (Figure 1A,C) (Williams et al., 2012). To visualize the dynamic changes in the shapes of all cells in tissue context at single cell during the gastrulation EMT, we sought to label the

membranes of all epiblast cells and perform time-lapse imaging. Time-lapse imaging of the epiblast cells in the vicinity of the primitive streak of developing mouse embryos is challenging for several reasons. Embryos need to be kept intact as tissues cannot be microdissected, the epiblast tissue is cup-shaped with inherent curvature and located within the deepest extremity of the embryo (up to 60µm away from the objective), needing to be imaged through the visceral endoderm and mesoderm tissue layers (Figure 1C). Even light-sheet systems, which by merging multi-view data can provide *in toto* visualization of cells in developing embryos, have predominantly been used with nuclear-localized reporters or scattered membrane-labelled cells, data which are less challenging to segment than widespread membrane-localized reporters (McDole et al., 2018).

We used a ZO-1-GFP protein fusion reporter (Foote et al., 2013) to visualize the tight junction and the apical surface of epiblast cells in order to quantify apical surface dynamics (Figure 1D); and a membrane-localized *R26*$^{mT/mG}$ reporter to visualize their entire plasma membrane and identify completion of apical constriction associated with cell ingression out of the epithelial layer (Figure 1-figure supplement 1A and Video S1). 3D time-lapse imaging of embryos at mid/late-streak stage (E7.5) was performed to image the primitive streak) (Figure 1A, B). Time-lapse imaging of ZO-1-GFP embryos revealed that epiblast cells undergo extensive rearrangements as cells on the left and right sides of the embryo converge towards the primitive streak (Figure 1D, Figure 1-figure supplement 1C, Video S2,3) (Williams et al., 2012). The majority of epiblast cells underwent apical constriction and ingression within a ~40µm region in the posterior midline (Figure 1D,E, Video S2), corresponding to the domain of Snail expression and basement membrane breakdown within the epiblast (Francou and Anderson, 2020; Ramkumar et al., 2016; Williams et al., 2012), which by convention defines the primitive streak (Figure 1E dotted lines). Rare apical constriction and ingression events were also observed outside the domain of the primitive streak (Figure 1-figure supplement 1B and Video S3 bottom).

Within a one hour period 44±2% of cells within the primitive streak domain, constricted and ingressed (mean±s.e.m., n=378 cells, 3 embryos) (Figure 1D,E,F, Video S2), with

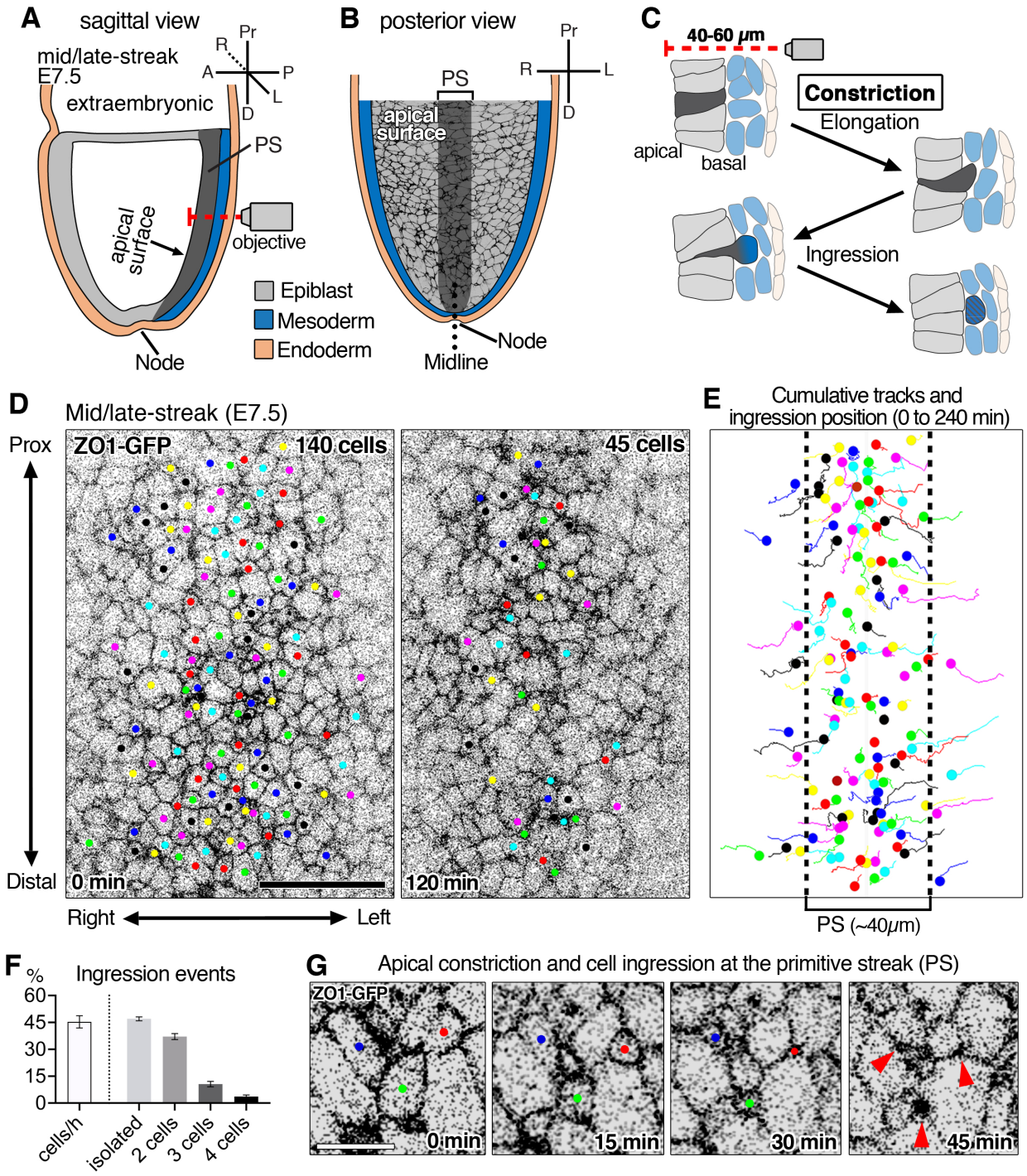

Figure 1: Time-lapse imaging of ZO-1-GFP reporter reveals EMT events at the primitive streak of the mouse gastrula and apical constriction associated with cell ingression. **(A)** Schematic sagittal section view of E7.5 mouse embryo and 3D time-lapse imaging performed from the posterior side with an objective positioned adjacent to the primitive streak (PS). Several tissue layers need to be imaged across (including visceral endoderm and mesoderm) to reach the epiblast apical surface situated furthest from the objective (red dashed line shows the microscope light path). **(B)** Schematic of a view of the epiblast layer apical surface from the

inner cavity. The midline (dotted line axis) separates the right and left sides of the embryo. **(C)** High magnification schematic of a sagittal view of an EMT event at the primitive streak depicting a cell constricting its apical surface, elongating basally (dark grey), and ingressing out of the epiblast layer to integrate the mesoderm (blue). Note the apical surface of epiblast cells is located 40-60μm away from the microscope objective. **(D)** Single time-points at t=0min and t=120min of a time-lapse of a ZO-1-GFP embryo. Movies were analyzed as maximum projections of z-stacks to visualize the apical surfaces of cells. Here all the cells that can be followed and observed ingressing during 4hr were tracked. Of 140 cells initially tracked, 95 cells constricted and ingressed over the course of 120min (45 tracked cells remaining). (Time lapse with 5min time interval, 290 cells in the field of view, 140 ingressing cells tracked). **(E)** Cumulative tracking of the 140 cells showing cell tracks over time (lines) and cell position during ingression event (dots). Epiblast cells converge toward the primitive streak (~40μm, dotted lines) where the majority of ingression events occur. **(F)** Graphs showing 44±2.1% of cells in the primitive streak ingress each hour, with 48±1.1% ingressing as single cells, 37±1.7% as pairs of cells, 11±1.5% as triplets (groups of 3 cells), and 4% as groups of 4 cells (of a total of 378 ingressing cells analyzed in 3 embryos). **(G)** High magnification view showing the apical constriction of 3 cells at the primitive streak.
Pr: proximal, D: distal, A: anterior, P: posterior, R: right, L: left, Ext Emb: extra embryonic region, PS: primitive streak. Error bars represent s.e.m. Scale bars, d, 40μm; g, 10μm.
Figure supplement 1: Apical constriction and ingression of epiblast cells in the vicinity of the mouse primitive streak.

ingression events appearing to occur stochastically (3-4h). Among the ingressing cells tracked, 48% constricted and ingressed as isolated events (more than 30min apart from adjacent neighboring cells), while the remaining 52% ingressed as pairs, and occasionally as groups of 3-4 cells (less than 30min apart from adjacent neighboring cells) (Figure 1F). At the tissue level the epiblast underwent extensive rearrangement, with some cells moving and acquiring new neighbors prior to their coordinate ingression (Figure 1-figure supplement 1D,E), while others, which were initially neighbors, ingressed at different times (more than 30 min apart) (Figure 1-figure supplement 1D,F).

Epiblast cells undergo a ratchet-like pulsed apical constriction during ingression

We next focused on changes associated with the apical surfaces of cells during their ingression. Apical constriction has been extensively studied in Drosophila, including during mesoderm formation and neuroblast delamination (An et al., 2017; Martin et al., 2009; Mason et al., 2013; Simoes et al., 2017), but few studies have investigated the

179 gastrulation EMT in an amniote, and it is unknown how cells constrict their apical surfaces
180 during single cell ingression in the mouse embryo versus the more global constriction and
181 invagination happening during Drosophila gastrulation. To follow changes in apical
182 surfaces during cell ingression, cell membranes were segmented using Tissue Analyzer
183 software (Aigouy et al., 2010; Aigouy et al., 2016) on projections of z-stacks from time-
184 lapse data. By visualizing cells at the primitive streak, we identified apical constriction
185 associated with cell ingression and quantified several parameters, including apical
186 surface area, apical cell surface elongation and orientation, and number of apical
187 junctions (Figure 1G, Figure 2,3-figure supplement 1, Video S4,5). Epiblast cells exhibited
188 a variety of apical surface sizes and shapes that fluctuated over time as they flowed
189 toward the primitive streak. As they initiated apical constriction at the primitive streak,
190 cells exhibited 20-80μm^2 apical surface area, and completed ingression within 25-90min
191 (Figure 2A and Figure 2,3-figure supplement 1B). With the time-scale we are to image
192 and keep living embryos and fluorescent signal integrity, majority of ingressing cells
193 exhibited pulsed constrictions, generally consisting of 2-4 major phases of contraction
194 (Figure 2B,C and Figure 2,3-figure supplement 1F). As cells progressed towards
195 ingression, their number of apical junctions decreased (Figure 2,3-figure supplement 1J,
196 Video S5).
197
198 A closer examination of individual cells allowed us to quantify features of apical surface
199 area throughout the constriction period. The example in Figure 2D depicts the apical
200 surface area of a cell exhibiting 3 main pulses of constriction each separated by more
201 stable intermediate steps (Figure 2C,D, Video S6). While cells showed an average rate
202 of constriction of 1.1±0.1 μm^2/min (mean±s.e.m., n=51 cells, 4 embryos), they exhibited
203 constriction pulses with higher rates of contraction (up to 4.6 μm^2/min), and an average
204 pulse magnitude of 1.4±0.1 μm^2/min (Figure 2B,C,E and Figure 2,3-figure supplement
205 1G). Cells at the primitive streak fluctuated between expansion and contraction before
206 ingression, as did epiblast cells located some distance from the streak (Figure 2C and
207 Figure 2,3-figure supplement 1B,E). During ingression, cells spent 90% of the time
208 contracting apical surfaces (compare with 48% and 55% for epiblast cells away from the
209 streak and before ingression) with an average rate of contraction of 1.1μm^2/min, higher

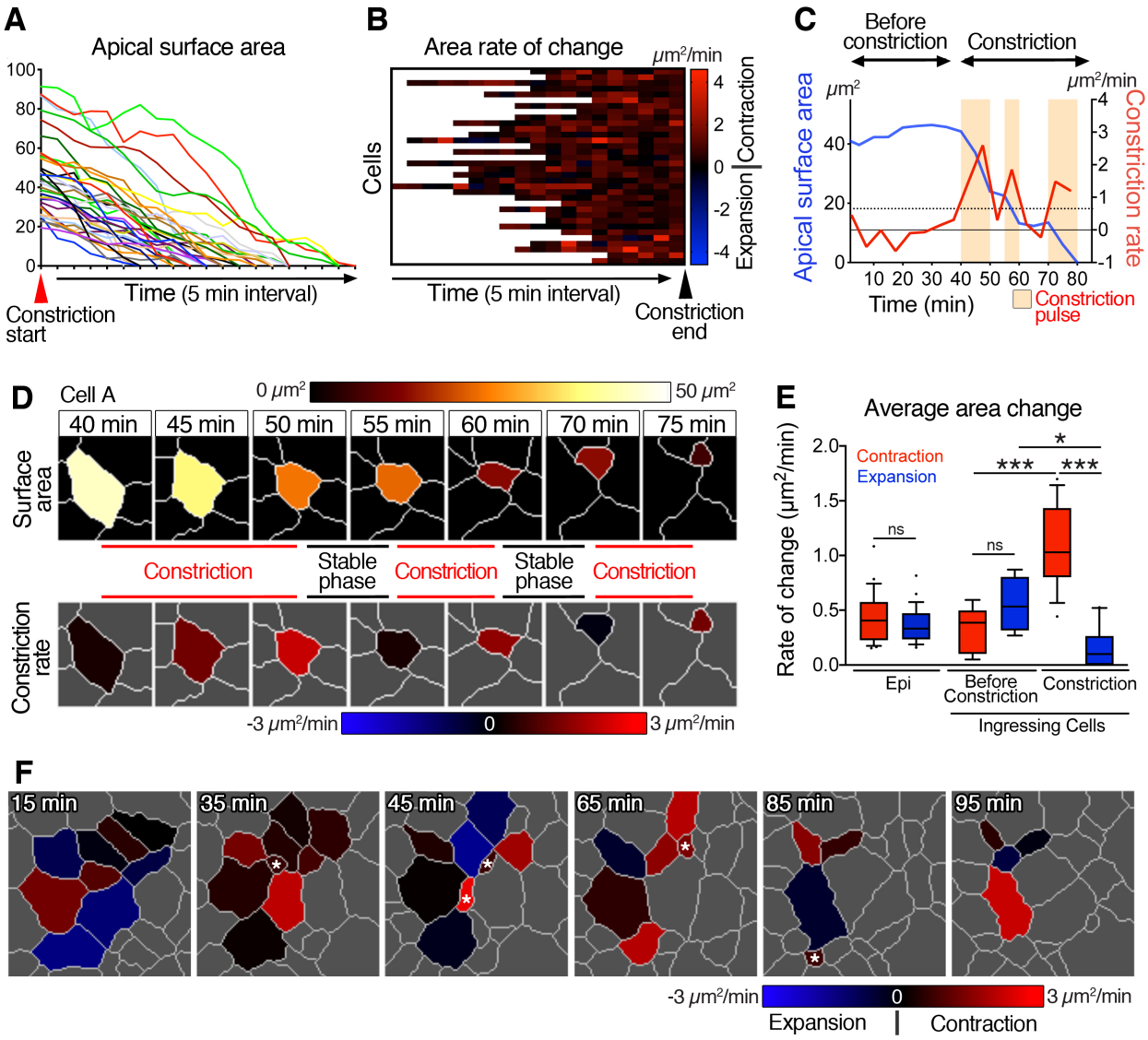

Figure 2: Pulsed racket-like apical constriction during epiblast cell ingression and asynchronous constriction at multi-cellular level. **(A)** Graph showing the apical surface area of a few cells during constriction associated with ingression, aligned to the start of constriction. **(B)** Heat map plot showing the rate of changes of apical surface area of cells during the final constriction period, revealing minimal expansion and pulsed contractions. Each row represents data for an individual cell and are aligned to the end of constriction. **(C)** Graph of apical surface area and rate of constriction of a single cell (cell A) showing slight oscillation in apical surface before undergoing a final constriction period with pulses of constriction, here with three main pulses (beige regions). **(D)** Membrane segmentation and color-coded time-series of apical surface area and constriction rate of a single cell (cell A) showing three pulses of constriction separated by stable steps. (cell corresponding to the plot showed in C). **(E)** Plot showing the average rate of area changes. Epiblast cells away from the primitive streak before ingression show low and equivalent levels of contraction and expansion. Cells at the primitive streak show no significant differences between contraction and expansion before the constriction, whereas rate of

contraction is significantly higher, and expansion reduces during the subsequent constriction period. **(F)** Color-coded time-series and heat map plot of rate of change of apical surface area showing asynchronous oscillation in area and asynchronous constriction and ingression among neighbors. Asterisks show ingression events.
51 cells quantified from 4 embryos. Error bars represent s.e.m. *P<0.05, ***P<0.001 (Unpaired bilateral Mann-Whitney test).
Figure supplement 1: Details and features of constriction pulses and cell parameters during constriction.
Figure supplement 2: Asynchronous apical constriction at the multi-cellular level.

than the average expansion rate of 0.1μm^2/min (Figure 2E and Figure 2,3-figure supplement 1D). To conclude, epiblast cells exhibited fluctuations in apical surface areas before ingression, and pulsed constrictions during ingression at the primitive streak. No hallmark or significant trend was observed at the onset of constriction, the elongation and orientation of the apical surface at the beginning or throughout the constriction period, nor the number of edges when constriction initiated (Figure 2,3-figure supplement 1J-L).

Asynchronous apical constriction at multi-cellular level

We analyzed clusters of cells at the primitive streak to uncover details of the apical constriction behavior at the multi-cellular level. Segmenting cell clusters allowed tracking of cells and documentation of changes in their apical surfaces through time, as cells ingressed (Figure 2F, Figure 2-figure supplement 2, Video S7). Cells underwent fluctuations in apical surface area as some cells constricted and ingressed (Figure 2-figure supplement 2B, Video S7). By color-coding and plotting the rate of apical change, we observed asynchronous oscillation of expansion and contraction phases among neighboring cells. As cells constricted and ingressed, the neighbors did not always exhibit the same behavior; some contracted at the same time, while others slightly expanded or maintained a constant surface area (Figure 2F, asterisk show ingression; S3C and Video S7). Thus, neighboring epiblast cells undergoing EMT and ingressing at the primitive streak displayed asynchronous apical behaviors and ingress in a stochastic-like manner, with some neighboring cells ingressing 2 hours apart, in comparison to Drosophila gastrulation where all ventral furrow cells constrict in less than 10min.

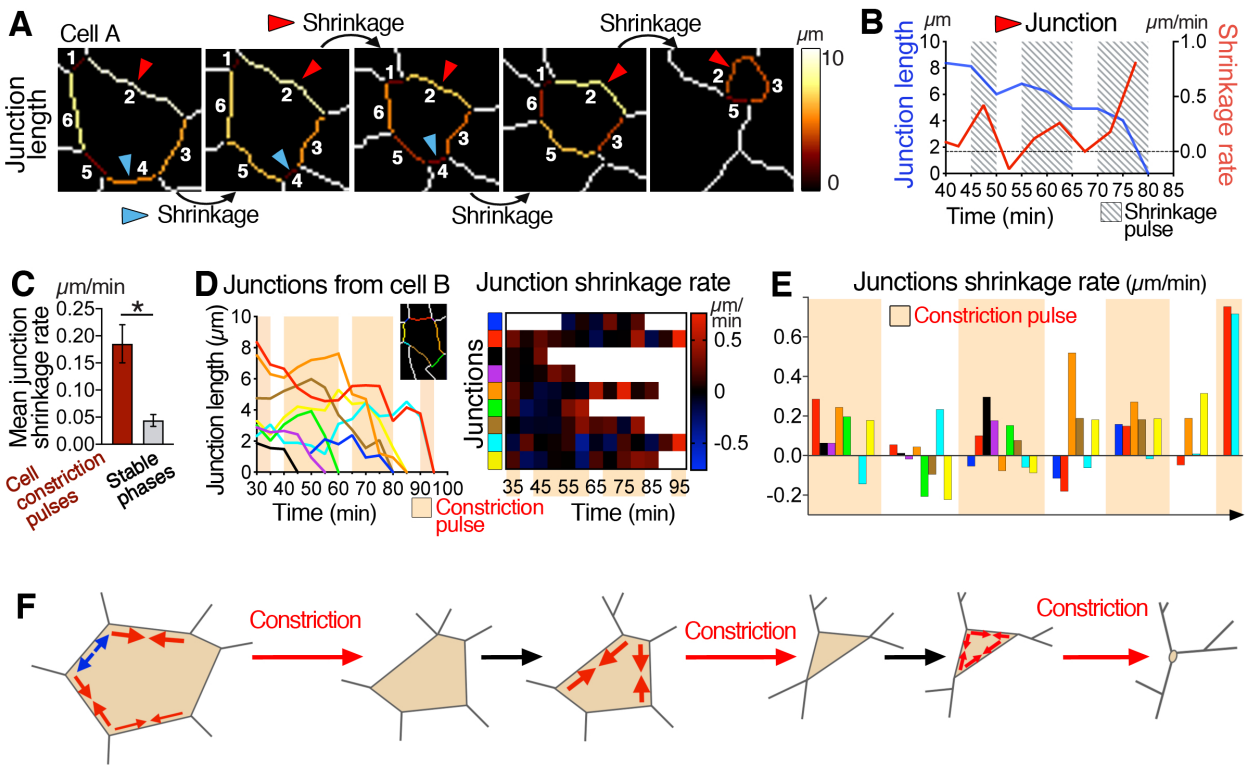

Figure 3: Asynchronous junctional shrinkage during apical constriction. **(A)** Membrane segmentation and color-coded time-series of single junction showing reduction of junctions length during apical constriction of cell A showed in Figure 2. Here the six initial junctions are numbered, and two are pointed (arrowheads) and shrink at different time. **(B)** Graph showing the length and rate of shrinkage of the junction identified with the red arrowhead in A, indicating the 3 main pulses of shrinkage (hatched regions). **(C)** Graph showing increased rate of junctional shrinkage during cell constriction pulses compare to stable phases between constriction pulses from multiple cells. **(D)** Graph showing the length of individual junctions (left) during apical constriction of a single cell (cell B plotted in Figure 2,3-figure supplement 1A). Junctions reduce their length differentially during the constriction pulses (beige regions). Heat map plot of the shrinkage rate of junctions (right), showing junctions shrinking asynchronously during the constriction pulses (beige time points). Each row represents data for an individual junction, junctions are color-coded as corresponding in the left plot and ordered as neighboring junctions. **(E)** Plot of the average shrinkage rate of each junction through time during each constriction pulse and stables phases, showing the asynchronous shrinkage of different sets of junctions with variable magnitude during the different cell constriction pulses. Junctions are color-coded as neighbors as in D. **(F)** Model of rachet-like pulsed constriction associated with asynchronous junctional shrinkage.
Error bars represent s.e.m. *P<0.05 (Unpaired bilateral Mann-Whitney test).

281

282 **Asynchronous shrinkage of junctions correlates with apical constriction during**
283 **cell ingression**

284 Most apical junctions of any given cell decreased in length in a pulsed manner, with 1-3
285 pulses of shrinkage (Figure 3A,B), with junctions appearing to shrink asynchronously
286 (Figure 3A,D, Video S6). By analyzing and quantifying the behavior of each junction of
287 any one cell during constriction, we noted that the average rate of shrinkage was
288 significantly higher during cell constriction pulses (Figure 3C). Junctions of individual cells
289 shrunk asynchronously (Figure 3D and Figure 2,3-figure supplement 1H,I), differentially
290 and with different magnitudes between one constriction pulse and the next (Figure 3E
291 and Figure 2,3-figure supplement 1H,I), suggesting that asynchronous differential
292 junctional shrinkage may trigger constriction of the cell surface. In sum, epiblast cells at
293 the mouse primitive streak constricted their apical surfaces in a ratchet-like manner, with
294 asynchronous shrinkage of junctions (Figure 3F).

295

296

297 **Anisotropic accumulation of components at apical junctions of epiblast cells**

298 We sought to analyze the localization of apical proteins implicated in epithelial apical
299 constriction in different tissues and species, that could potentially be involved in the apical
300 constriction associated with the mouse gastrulation EMT. E7.5 embryos were
301 immunostained and epiblast apical surface imaged in regions proximo-distally middle of
302 the primitive streak (least curved and best for analysis) (Figure 4-figure supplement 1A).
303 Crumbs2 and Myosin2B have been described as exhibiting heterogenous and
304 complementary distributions at the apical junctions of epiblast cells (Ramkumar et al.,
305 2016), and our data showed Myosin2B and Crumbs2 were predominantly anisotropically
306 distributed, with Crumbs2 exhibited a stronger anisotropy being almost absent from some
307 junctions, and Myosin2B observed on all junctions but at varying levels (Figure 4B and
308 Figure 4-figure supplement 1B).

309

310 We next investigated the localization of other apical proteins, including the actomyosin
311 components, mono- and di-phosphorylated Myosin Light Chain (pMLC and ppMLC),

312 Rock1, a Rho-associated kinase that phosphorylates and activates myosin light chain,
313 and F-actin. We analyzed the localization of the Crumbs complex proteins PatJ, and
314 aPKC, a regulator of non-muscle Myosin2 contexts (Biehler et al., 2021; Petrov et al.,
315 2017; Roper, 2012; Sidor et al., 2020). Membrane segmentation allowed us to
316 systematically quantify several parameters, including apical surface area, cell elongation,
317 and the intensity of junctional protein accumulation (Figure 4A, Figure 4-figure
318 supplement 1C). Two parameters were calculated based on junctional protein intensity
319 and used to evaluate the level of anisotropy: the standard deviation of the junctional
320 intensity measurements cells (SD), and the ratio of the maximum to minimum junctional
321 intensity values (Max/Min) for each cell (Figure 4A). The membrane-GFP reporter served
322 as a control for homogeneous membrane fluorescence localization with low anisotropy
323 and the cohort of proteins analyzed exhibited different degrees of anisotropy (Figure 4B,C
324 and Figure 4-figure supplement 1D,E) . Some proteins such as Crumbs2, ppMLC,
325 ROCK1 and ZO-1 showed a high level of anisotropy (Figure 4B,C and Figure 4-figure
326 supplement 1D,E), though each exhibited a distinct pattern. ZO-1 was observed on all
327 junctions, with variable intensity. Crumbs2 was present on some junctions but absent on
328 others. ppMLC and ROCK1 also exhibited accumulation on some junctions, but low
329 accumulation on others. Other proteins, including PatJ and F-actin, displayed distinct
330 patterns but intermediate anisotropy. Finally some proteins, such as pMLC, Myosin2B
331 and aPKC showed less anisotropy with lower SD and Max/Min values (Figure 4B,C and
332 Figure 4-figure supplement 1D,E). These data allowed us to classify proteins based on
333 their distribution and level of anisotropy. Staining observed at earlier (E7) and later stages
334 (E8) did not show visible differences (data not shown) (Ramkumar et al., 2016).
335
336 The anisotropic membrane accumulation of proteins is relevant with respect to the planar
337 cell polarity (PCP) of epithelial cells. The apical proteins we analyzed did not show a
338 visible planar polarized distribution, which we sought to verify quantitatively.
339
340
341
342

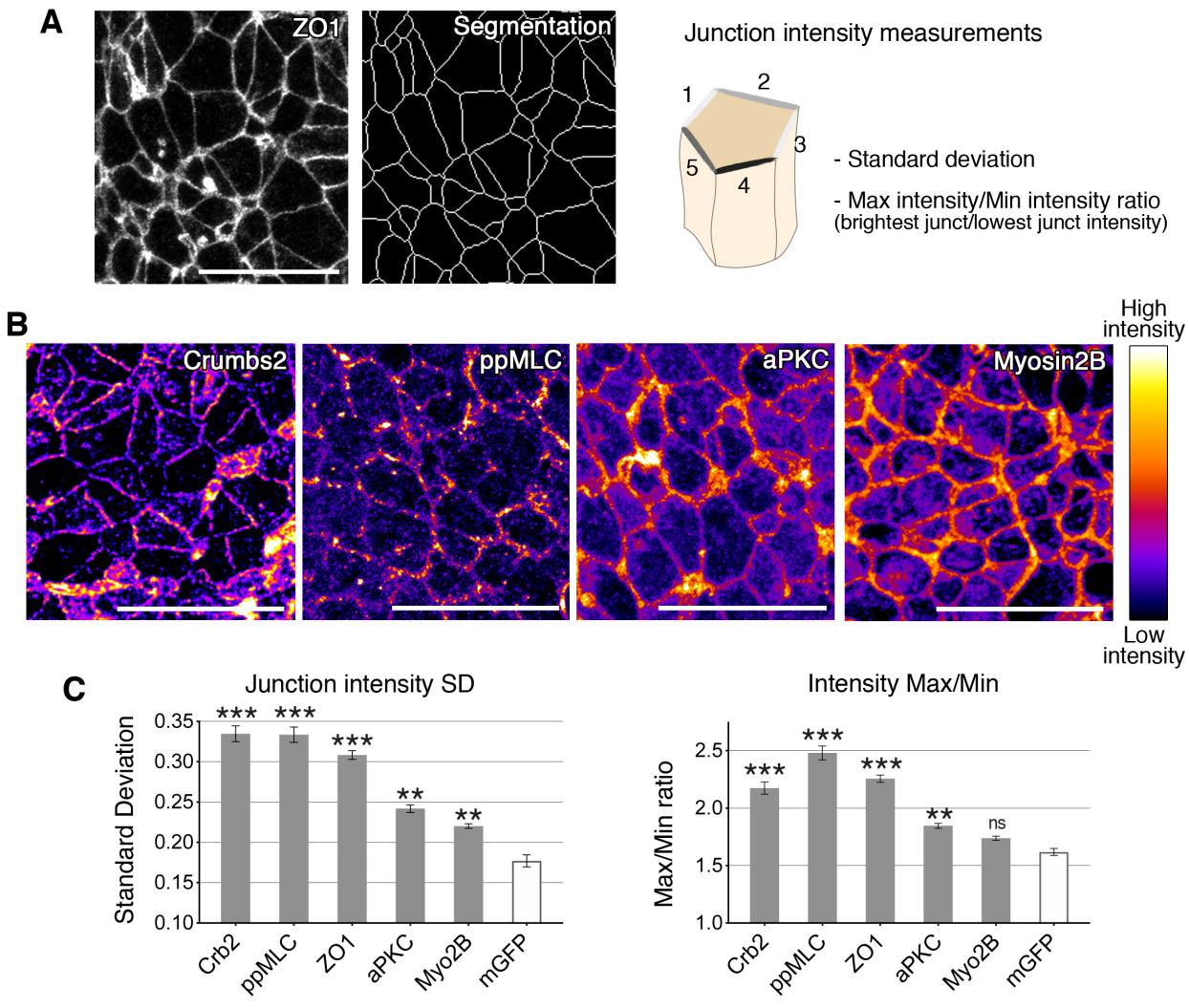

Figure 4: Anisotropic distribution of apical components in epiblast cells at the primitive streak. **(A)** ZO-1 apical membrane localization and corresponding skeleton of membrane segmentation used to quantify junctional intensities and anisotropy parameters as schematized. The average intensities of proteins associated with the junctions of individual cells are used to calculate the standard deviation between junctions, and the difference between junctions with the maximum and minimum intensities. **(B)** Lookup table (LUT) of immunostaining of Crumbs2, di-phosporylated Myosin Light Chain (ppMLC), aPKC and Myosin2B. These proteins show different distributions at apical junctions. Myosin2B and aPKC are present on almost every junction and seem to have a low anisotropy distribution, whereas ppMLC and Crumbs2 are not present on every junction and show a more anisotropic distribution. **(C)** Plots showing the anisotropy parameters, standard deviation and max/min. Proteins such as Crumbs2, ZO-1 and ppMLC show elevated parameters corresponding to a high level of anisotropy, whereas aPKC and Myosin2B show lower anisotropy. The membrane-GFP (recombined mTmG mouse reporter line) is used as control showing homogeneous distribution across all junctions and low anisotropy. (a range of 372- 612 junctions were analyzed in 3 -4 embryos for each protein. Statistical test compare each proteins to mGFP).

360 Pr: proximal, D: distal, R: right, L: left, PS: primitive streak. **P<0.01, ***P<0.001 (Unpaired
361 bilateral Mann-Whitney test). Error bars represent s.e.m. Scale bars, 20μm.
362 **Figure supplement 1**: Complementary accumulation of Crumbs2 and Myosin2B, and
363 anisotropy of apical components at the primitive streak.
364 **Figure supplement 2**: Apical proteins show anisotropy accumulation but no planar polarity
365
366
367 We compared the planar polarity index calculated by Tissue Analyzer (amplitude and
368 orientation of polarity) and mean junctional intensity in relation to junction orientation
369 (Figure 4-figure supplement 2) (two ways to assess planar polarity) of apical proteins
370 analyzed to Celsr1, a protein implicated in PCP in mouse and chick (Curtin et al., 2003;
371 Mahaffey et al., 2013; Nishimura et al., 2012). Celsr1 exhibited a planar polarized
372 localization and tended to accumulate on junctions oriented on left-right axis
373 perpendicular to the proximo-distal axis, but by contrast, Myosin2B, Crumbs2, ppMLC,
374 ZO-1 and aPKC, showed no specific axis of planar polarity.
375
376
377 **Reciprocal distribution of apical proteins at apical junctions**
378 We next assessed the colocalization and correlation of the different apical proteins at
379 junctions. Segmentation and intensity values, which served as a readout of concentration,
380 were used to systematically compare mean junctional protein intensities and correlate
381 localization. Some proteins such as ppMLC (di-phosphorylated Myosin Light Chain) and
382 Rock1 showed similar patterns with comparable levels of anisotropy, and appeared to
383 accumulate on the same junctions (Figure 5A). Co-staining revealed a broader
384 accumulation for ppMLC. However, where Rock1 was seen to accumulate, ppMLC was
385 always present, demonstrating strong colocalization (Figure 5A,5C), close to that
386 observed with a positive control staining for ppMLC with two distinct secondary antibodies
387 (Figure 5C and Figure 5-figure supplement 1C,E). F-actin accumulated on most junctions,
388 exhibiting a distinct distribution from ppMLC, whereas F-actin and ppMMLC exhibited a
389 high level of colocalization (Figure 5-figure supplement 1A), with high correlation of
390 junctional intensities (Figure 5C and Figure 5-figure supplement 1A,E). Comparison of F-
391 actin and Rock1 revealed a similar high correlation (Figure 5-figure supplement 1D,E).
392 Thus, the correlated distributions of ppMLC, Rock1 and F-actin proteins suggests they

393 could function at the same junctions. Despite exhibiting anisotropy, ZO-1 and aPKC were
394 observed to be present on all junctions (Figure 4A,B and S3), with a high level of
395 correlation, similar to a positive control (Figure 5-figure supplement 1D,E), demonstrating
396 their accumulation on the same junctions.
397
398 By contrast, when comparing other junctional proteins, we observed very low or no
399 correlation. Crumbs2 and Myosin2B exhibited a complementary localization (Figure 5B),
400 with minimal colocalization. Comparisons of Crumbs2-Myosin2B junctional intensities
401 revealed a broad distribution and very low correlation (Figure 5B,C). Comparing PatJ, a
402 Crumbs partner protein, with pMLC (phosphorylated-Myosin Light Chain) showed a
403 similar accumulation with almost no correlation (Figure 5C and Figure 5-figure
404 supplement 1B,E). Analysis of other protein pairs, including ZO-1-ppMLC, and aPKC-
405 ppMLC revealed low correlation (Figure 5-figure supplement 1D,E).
406
407 To gauge the non-complementarity and assess potential anti-correlation of certain
408 proteins, we analyzed junctional intensity correlations grouped by individual cells, rather
409 than junctions collectively. This analysis confirmed the strong correlation of ppMLC,
410 Rock1 and F-actin, where most cells exhibited a positive correlation trend with a high
411 correlation coefficient (Figure 5-figure supplement 2A,B). For pairs of proteins such as
412 Crumbs2 and Myosin2B, and PatJ and pMLC, which showed no correlation when junction
413 quantifications were compared (Figure 5B,C and Figure 5-figure supplement 1), grouping
414 junction intensities by individual cells revealed a broad distribution; some cells showed
415 anti-correlation, some no correlation and some positive correlation (Figure 5-figure
416 supplement 2C-F). This analysis illustrated a heterogeneity across the epiblast population
417 in the vicinity of the primitive streak, at any one time, supporting our hypothesis that
418 anisotropic accumulation patterns are dynamic.
419
420 These quantitative analyses of apical protein anisotropy patterns combined with the
421 correlation of distributions, allowed us to define two groups of proteins that tend to
422 accumulate on different junctions. Cytoskeletal proteins including Myosin2,
423 phosphorylated MLC, ROCK1 and F-actin predominantly accumulate on the same

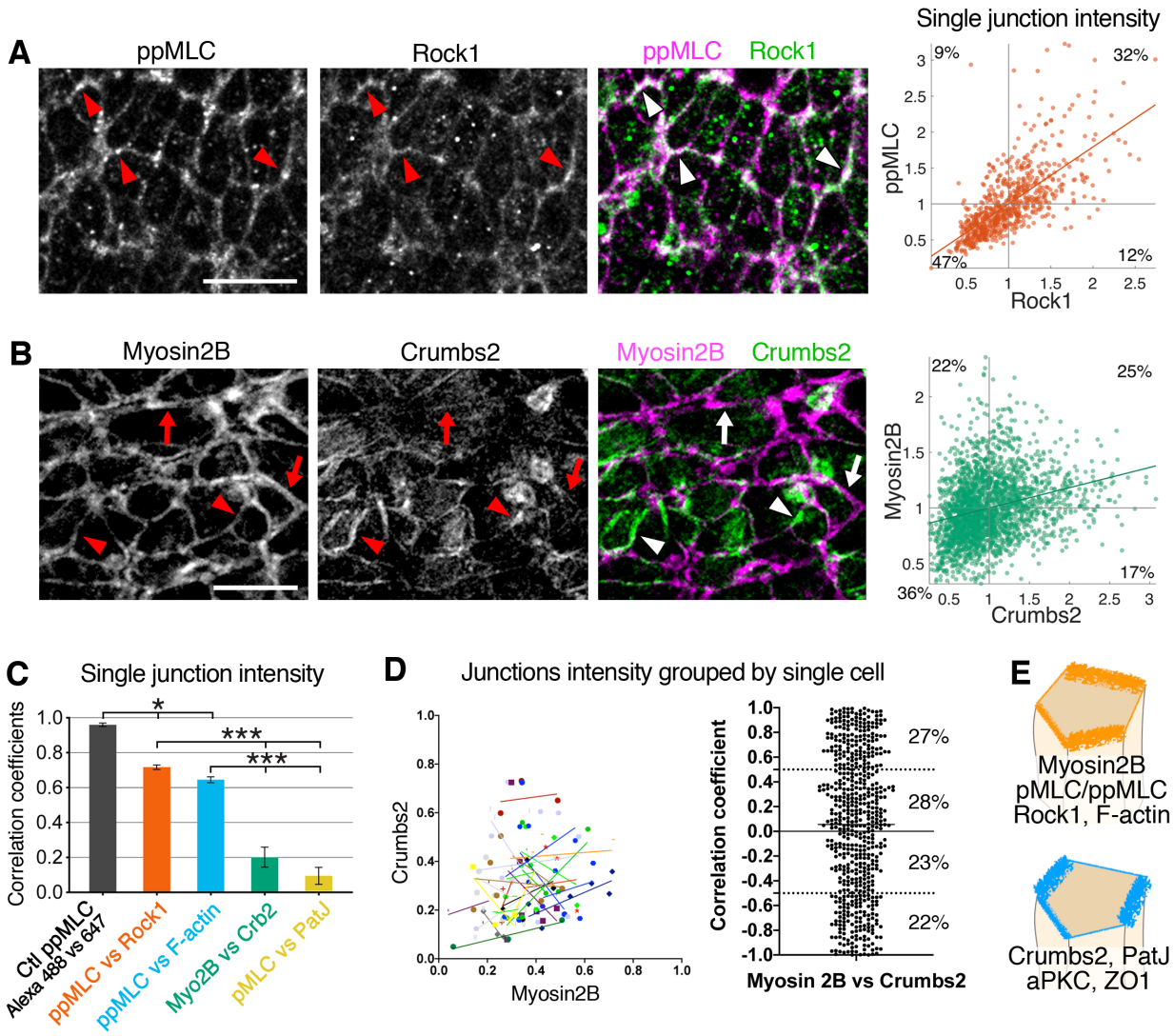

Figure 5: Complementarity accumulation of apical components at apical junctions. **(A)** Co-immunostaining of ppMLC and Rock1 reveals a tendency to accumulate on the same junctions. Note colocalization of fluorescent signal on most junctions (arrowheads). Scatter plot on the right showing elevated intensity correlation of the two proteins. Each point represented the mean intensity at a single junction. **(B)** Co-immunostaining of Myosin2B and Crumbs2 reveals that they tend to accumulate on different junctions. Note junctions where Myosin accumulation predominates (arrows), and junctions where Crumbs2 predominates (arrowheads). Corresponding scatter plot shows a low correlation. **(C)** Plot showing the correlation coefficients associated with the different scatter plots. Proteins such as ppMLC, Rock1 and F-actin exhibit a strong correlation with a high coefficient (ppMLC vs Rock1=0.72±0.01, ppMLC vs F-actin=0.65±0.02), whereas others including Myosin2B and Crumbs2, PatJ and pMLC exhibit much lower correlation with low coefficient (Myosin2B vs Crumbs2=0.20±0.06, pMLC vs

437 PatJ=0.09±0.05). **(D)** Example of scatter plot showing the junctional intensity correlation of
438 Crumbs2 and Myosin2B in a cohort of cells. Each symbol represents one junction, grouped by
439 cells (color coded) with respective correlation trends, depicting a mix of cells with correlation,
440 some with no correlation, and some with anti-correlation. Graph on the right shows correlation
441 coefficients for a larger number of cells, showing a broad distribution, from correlation (+1) to
442 anti-correlation (-1). % show the distribution of correlation coefficients in the different quarters.
443 **(E)** Based on co-staining for multiple apical proteins and measurements of anisotropy and
444 correlation, two groups of proteins can be defined with a tendency to accumulate on same
445 junctions: actomyosin components, and apical determinants and junctional proteins.
446 711-1448 junctions were quantified in 3-4 embryos for each pair of proteins. *P<0.05,
447 ***P<0.001 (one-way ANOVA test). Error bars represent s.e.m. Scale bars, 10μm.
448 **Figure supplement 1**: Correlation of protein distributions at apical junctions.
449 **Figure supplement 2**: Junctional correlation of proteins at the single cell level.
450
451
452 junctions, while apical components and junctional proteins such Crumbs2, PatJ, aPKC,
453 ZO-1 will co-localized on other junctions (Figure 5D). This anisotropic distribution of the
454 actomyosin network and Crumbs-complex associated proteins is associated with
455 dynamic apical constriction.
456
457
458 **Cellular defects in *Crumbs2*$^{-/-}$ mutant embryos at the primitive streak**
459 Crumbs2 is an important regulator of the mouse gastrulation EMT, where it promotes cell
460 ingression. Epiblast cells fail to ingress and accumulate at the primitive streak in *Crb2*$^{-/-}$
461 embryos (Ramkumar et al., 2016). By quantifying the apical surface of posterior epiblast
462 cells at E8.0, we observed increased cell density and cells with smaller apical surfaces
463 around the primitive streak of mutants, as compared to littermate controls (Figure 6,7-
464 figure supplement 1A). This cell crowding was not observed half a day earlier at E7.5
465 (Figure 6,7-figure supplement 1B) (Ramkumar et al., 2016) when mutant embryos were
466 morphologically indistinguishable from wild-type stage-matched counterparts.
467 Morphological defects (apical surface areas and surface elongation) in cells at the
468 primitive streak were first detected at E8.0 with cells having smaller and rounder apical

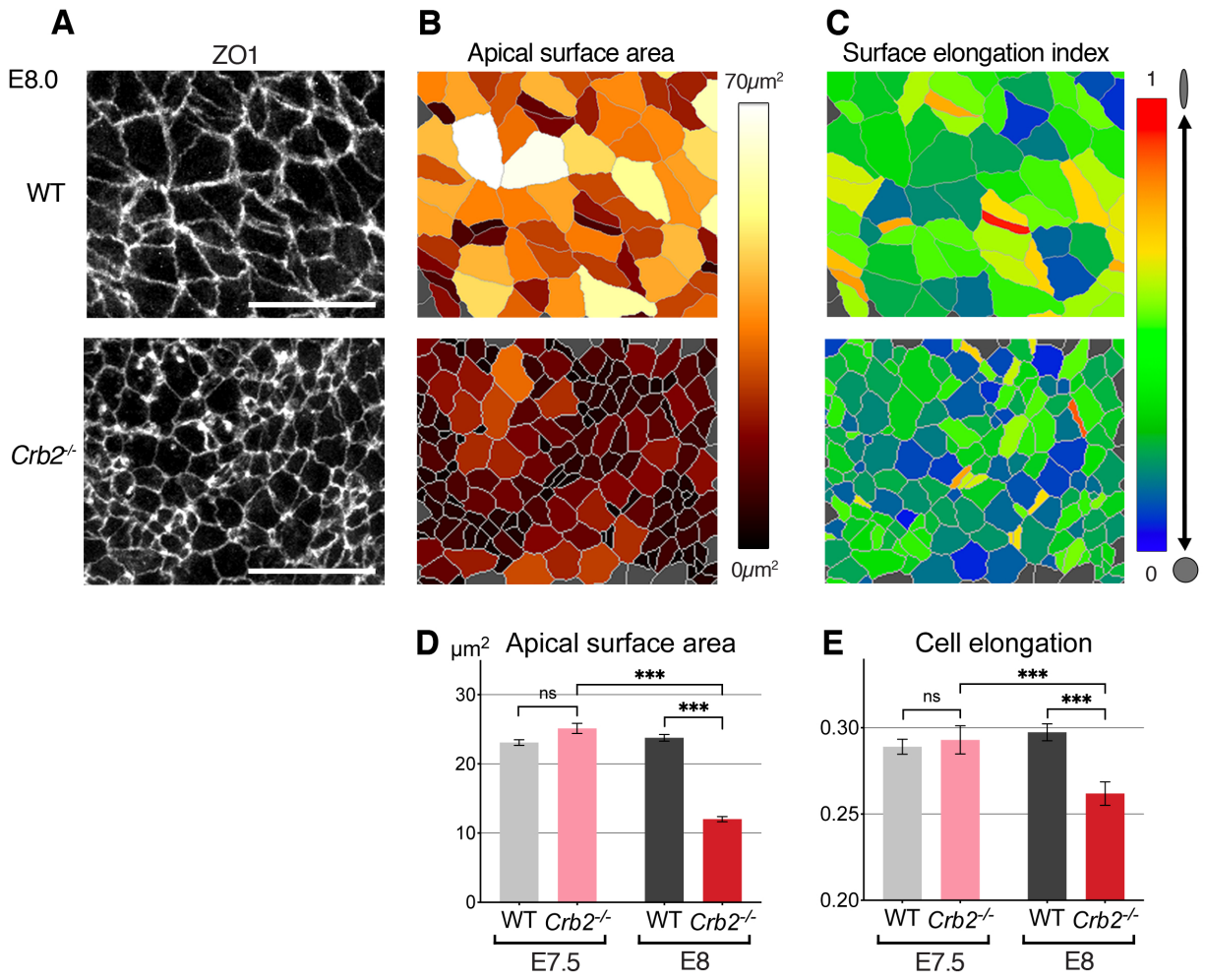

Figure 6: Cellular defects in Crumbs2 mutant embryos at the primitive streak. **(A)** ZO-1 immunostaining showing the apical surface of WT and *Crumbs2* mutant embryos at E7.5 and E8.0. **(B)** Segmentation and color code of apical surface areas reveals smaller surfaces in *Crumbs2* mutants at E8.0. **(C)** Color code of cell surface elongation index calculated by Tissue Analyzer (regardless of their axis) reveals rounder surfaces in *Crumbs2* mutants at E8.0. **(D)** Graph of quantifications showing significantly smaller apical surfaces in *Crumbs2* mutants at E8.0 compared to E7.5, and to WT embryos. **(E)** Graph showing significantly less elongated apical surfaces in *Crumbs2* mutants at E8.0 compared to E7.5, and to WT embryos. 334-1187 cells from 3-5 embryos were quantified for each genotype and stage. ***P<0.001 (Unpaired bilateral Mann-Whitney test). Error bars represent s.e.m. Scale bars, 20μm.

surfaces (Figure 6A-E and Figure 6,7-figure supplement 1B) resulting from their failure to ingress, and consequent accumulation in the epiblast.

486 **Molecular defects in *Crumbs2*$^{-/-}$ mutant embryos precede cellular defects**
487 To identify molecular defects associated with and preceding the ingression defect we
488 analyzed the distribution of actomyosin components in *Crb2*$^{-/-}$ embryos. Although ZO1
489 distribution appeared unchanged in the mutants, suggesting the integrity of junctions was
490 not altered, we observed reduced levels of Myosin2B and ppMLC (the fully activated form
491 of Myosin Light Chain) in mutants at E7.5 (Figure 7A,B) and Figure 6,7-figure supplement
492 1C). We also observed more diffuse and reduced cortical actin filaments at the apical
493 junctions of epiblast cells in mutants, whereas the medial pool of actin appeared slightly
494 increased (Figure 7A,B). Thus, actomyosin apical accumulation and activity were
495 perturbed without alteration of junctional integrity in *Crb2*$^{-/-}$ embryos at E7.5, preceding
496 morphological defects.
497
498 We next focused on aPKC and Rock1, implicated in the regulation of the actomyosin
499 network by Crumbs in Drosophila and cultured cells (Biehler et al., 2021; Ishiuchi and
500 Takeichi, 2011; Roper, 2012; Sidor et al., 2020). By quantifying the intensity of aPKC and
501 Rock1 at junctions, we observed a 3-fold reduction of aPKC intensity at apical junctions
502 and a more diffuse signal in the cytoplasm, and we observed a slight reduction of
503 junctional Rock1 (Figure 7C and Figure 6,7-figure supplement 1D). These observations
504 suggest a network with aPKC and Rock1 regulating actomyosin downstream of Crumbs2.
505 By quantifying the two parameters used to assess anisotropic distributions at apical
506 junctions, we observed that in *Crb2*$^{-/-}$ embryos the SD and Max/Min of junction intensity
507 of Myosin2, F-actin ZO-1, aPKC and Rock1 was reduced (Figure 7D), revealing reduced
508 anisotropy and more homogenous distribution of these proteins.
509
510
511
512

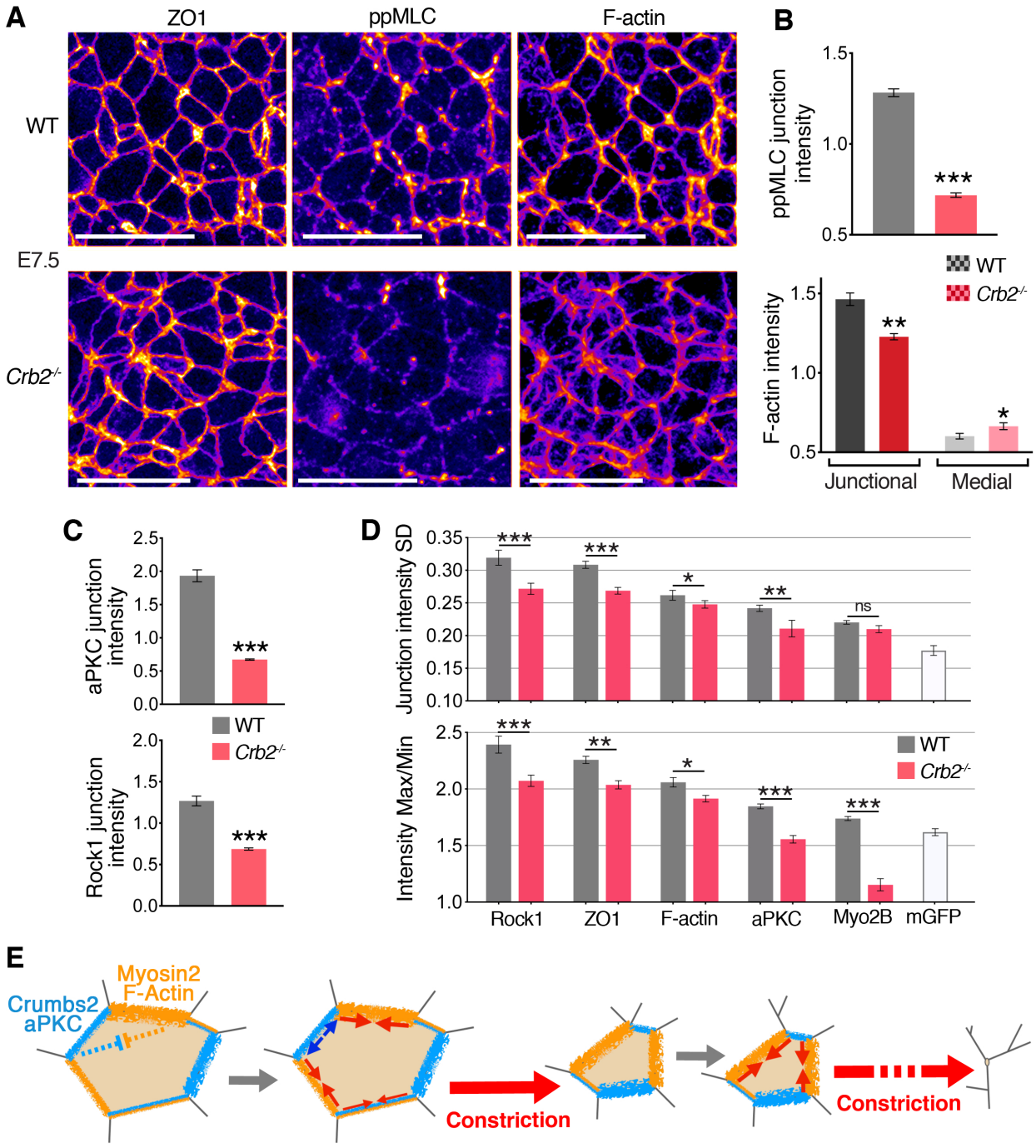

Figure 7: Molecular defects in *Crumbs2* mutants preceding visible cellular defects. **(A)** Co-immunostaining for ZO-1, ppMLC and F-actin in WT and *Crumbs2* mutants at E7.5 reveal reduced ppMLC and F-actin junctional intensities. **(B)** Plots showing intensity measurements of junctional ppMLC and F-actin. ppMLC shows significant decrease in junctional accumulation in *Crumbs2* mutants. F-actin shows lower junctional accumulation and increased diffuse medial intensity in *Crumbs2* mutants. **(C)** Graphs of junctional intensity measurements showing significantly decreased aPKC and Rock1 intensity in *Crumbs2* mutants compared to WT. **(D)** Anisotropy parameters, Standard Deviation and Max/Min showing perturbed junctional

522 accumulation anisotropy in *Crumbs2* mutants compared to WT embryos. ZO-1, F-actin,
523 Myosin2, aPKC and Rock1 show reduced anisotropy in *Crumbs2* mutants. **(E)** Working model.
524 Actomyosin network and Crumbs2 complex show anisotropic and complementary distribution at
525 apical junctions of epiblast cells at the primitive streak. These distributions are likely dynamic
526 through time and heterogenous among cells, and could potentially regulate each other
527 distribution. Junctions asynchronously shrink and allow ratchet-like constriction of apical
528 surfaces, facilitating cell constriction and ingression without creating increased tension within
529 the tissue.
530 334-1187 cells in 3-5 embryos were quantified for each genotype and stage. *P<0.05, **<0.01,
531 ***P<0.001 (Unpaired bilateral Mann-Whitney test). Error bars represent s.e.m. Scale bars,
532 20μm.
533 **Figure supplement 1**: Cellular and molecular defects in *Crumbs2* mutant embryos.
534
535
536
537 **DISCUSSION**
538
539 To develop a dynamic mechanistic understanding of the mouse gastrulation EMT at
540 cellular resolution and tissue-scale we 3D time-lapse imaged *ex utero* cultured embryos.
541 We used membrane tagged reporters and quantified the spatiotemporal features of apical
542 cell surfaces, junctions and junctional composition of cells in the vicinity of the primitive
543 streak. Our analyses reveal that after converging at the primitive streak, epiblast cells
544 undergo EMT, either individually or in small groups of cells, in what appear to be
545 stochastic events. Cells constrict their apical surfaces in a ratchet-like manner during
546 ingression from the epiblast epithelium. Constriction is associated with the anisotropic
547 apical distribution of actomyosin network and Crumbs2 complex proteins.
548
549 Apical constriction is an evolutionarily conserved behavior associated with gastrulation in
550 invertebrates such as Drosophila, nematodes and sea urchins, as well as in vertebrates
551 and amniotes, such as Xenopus and chick (Christodoulou and Skourides, 2015; Lecuit
552 and Lenne, 2007; Martin and Goldstein, 2014; Martin et al., 2009; Rozbicki et al., 2015).
553 We observed fluctuations in the size and shape of the apical surface of epiblast cells as
554 they converged towards the streak. In the vicinity of the streak, and as cells ingressed,
555 their apical surfaces predominantly constricted, in a step-wise ratchet-like manner.
556

557 Pulsed ratchet-like apical constrictions have been observed in Drosophila gastrulation,
558 where cells at the ventral furrow constrict in a short period of time to drive tissue
559 invagination, followed by en-masse cell delamination (Martin et al., 2009; Mason et al.,
560 2013). Drosophila neuroblast delamination also exhibits a ratchet-like apical constriction
561 (An et al., 2017; Simoes et al., 2017). Despite these similarities, mesoderm formation
562 process during gastrulation of Drosophila and mouse cannot be directly compared as they
563 exhibit different time-scales, mechanisms and spatial parameters. In Drosophila the entire
564 ventral furrow constricts in less than 10min, triggering a tissue-wide invagination without
565 cell ingression, thereafter cells lose their epithelial properties and form a mesenchymal
566 mesodermal tissue. By contrast, in the mouse embryo epiblast cells at the primitive
567 undergo constriction and ingression in a more isolated fashion over the course of almost
568 2 days. Our time-lapse imaging revealed a ratchet-like apical cell constriction operating
569 in the mouse gastrulation EMT, where cells predominantly ingress as isolated cells or
570 small cluster, versus the en-masse constriction and invagination taking place in
571 Drosophila.
572
573 We further demonstrated that this apical constriction is associated with the asynchronous
574 contraction of junctions between neighboring cells, potentially regulated by the apical
575 actomyosin network. During Drosophila gastrulation, an apico-medial network of
576 actomyosin pulls apical cell junctions to simultaneously reduce their length and allow the
577 constriction of apical surface of cells at the ventral furrow (Coravos and Martin, 2016;
578 Martin et al., 2009; Mason et al., 2013). Drosophila neuroblasts exhibit polarized apical
579 constriction driven by both planar polarized junctional and medial actomyosin networks,
580 predominantly leading to a loss of antero-posterior junctions (Simoes et al., 2017). In the
581 mouse gastrula, we found that cells undergoing EMT contract and lose cell-cell junctions
582 in an asynchronous manner without apparent planar polarity. Our analyses of the
583 junctional distribution of Myosin2 supports its potential involvement in regulating
584 constriction during ingression, but does not exclude an additional role played by a medial
585 pool. Pulsed actomyosin activity has been documented in various processes involving
586 cell shape changes, including epithelial apical constriction (Coravos et al., 2017; Heer
587 and Martin, 2017; Martin and Goldstein, 2014). The pulsed constriction we observe in

588 mouse gastrulation indicates conservation of this actomyosin behavior, as a general
589 mechanism that integrates assembly and disassembly of the network and rearrangement
590 and recruitment of Myosin and Actin molecules. Furthermore, pulsed contractility could
591 allow a substantial but transient constriction of epiblast apical surfaces during ingression
592 without creating deleterious tension which could impact the integrity of the tissue.
593
594 Since large numbers of cells undergo EMT and leave the epiblast epithelium at any given
595 time, simultaneous constriction and ingression of multiple neighboring cells could exert
596 extreme tension and deformation in the tissue. Our observation of a stochastic and
597 asynchronous constriction of neighboring cells provides a parsimonious explanation for
598 maintaining epithelial integrity, and a continuation of ingression events at the primitive
599 streak and tail bud for almost 2 days throughout gastrulation, in comparison to Drosophila
600 gastrulation where all ventral furrow cells constrict in less than 10min. Cell division taking
601 place on the basal side of an epiblast layer, has been reported at the primitive streak
602 where it has been proposed to facilitate cell ingression (Mathiah et al., 2020). Apical
603 constriction and basal cell division could therefore work in concert to promote the correct
604 number of cell ingression events.
605
606 Myosin2 is a driver of membrane movement and apical constriction in various contexts
607 (An et al., 2017; Chung et al., 2017; Marston et al., 2016; Martin and Goldstein, 2014;
608 Martin et al., 2009; Mason et al., 2013; Nishimura et al., 2012; Roh-Johnson et al., 2012;
609 Samarage et al., 2015; Simoes et al., 2017). Crumbs2 is involved in the EMT process
610 during mouse gastrulation and exhibits a complementary localization to Myosin2
611 (Ramkumar et al., 2016) (our data). Anisotropic membrane localization of Crumbs has
612 been implicated in Drosophila salivary gland development, where it controls the
613 localization of actomyosin cables at the placode border, necessary for apical constriction
614 and tissue invagination (Roper, 2012). Recently, Crumbs has also been implicated in
615 apical constriction during neuroblast cell ingression in Drosophila (Simoes et al., 2022).
616 We observed the anisotropic and complementary localization of Crumbs2 and Myosin2,
617 and have identified other proteins exhibiting anisotropic distributions. Although Myosin2B,
618 F-actin, aPKC and ZO-1 are present on all apical junctions, they exhibit a differential

619 anisotropic accumulation between the junctions of any one cell. Other proteins such as
620 ppMLC and the myosin kinase Rock1, as well as Crumbs2 and its partner PatJ, exhibited
621 a higher level of anisotropy. In the Drosophila salivary gland placode border, Crumbs and
622 Myosin2 show planar polarized localization with Crumbs being absent from cell junctions
623 that contact the border of the placode, allowing the accumulation of myosin II at the
624 placode border and formation of a supracellular actomyosin cable (Roper, 2012). By
625 contrast, our results in mouse show that Crumbs2, Myosin2B and several other proteins
626 do not exhibit planar polarity, but what appears to be a disordered anisotropy. Our studies
627 reveal a patterned distribution in which actomyosin regulators and Crumbs2, aPKC and
628 ZO-1 accumulate on subsets of cell junctions and display complementary distributions.
629 We propose that these anisotropic patterns are dynamic and control the asynchronous
630 junction contraction associated with apical constriction.
631
632 Crumbs2 acts through aPKC and Rock to regulate Myosin2 localization in the *Drosophila*
633 salivary gland (Roper, 2012), and aPKC has been shown to regulate Myosin2 junctional
634 localization and activity both positively and negatively in different context, directly or
635 through other proteins (Biehler et al., 2021; Ishiuchi and Takeichi, 2011; Petrov et al.,
636 2017). The regulation of Myosin2 by Crumbs and aPKC through Rock in *Drosophila*
637 salivary gland development is complex (Sidor et al., 2020), and despite Rock membrane
638 association being tightly regulated by Crumbs across the tissue, regionally distinct
639 behaviors have been observed. At placode borders, cells exhibit a polarized accumulation
640 of Crumbs/aPKC and Rock to control actomyosin cable formation, whereas in the center,
641 where cells constrict during the tissue invagination, both Crumbs and Rock are
642 isotropically present at junctions (Chung et al., 2017; Sidor et al., 2020). Our results
643 demonstrate that during mouse gastrulation Crumbs2 controls the apical accumulation
644 and activity of actomyosin, which could account for the defects in apical constriction and
645 ingression in Crumbs2 mutants. We observed Crumbs2 as required for the correct
646 accumulation and distribution of aPKC, Myosin2, Rock1 and F-actin at apical junctions,
647 without alteration of junctional integrity. Crumbs2 along with aPKC could control the
648 anisotropic accumulation of actomyosin, triggering asynchronous junctional reduction
649 resulting in apical constriction during ingression (Figure 7E).

650

651 In ingressing mouse epiblast cells Crumbs2 together with aPKC and Rock1 could
652 represent a complex network implicating other proteins, required for Myosin2 localization
653 and activity at the apical membrane, but also potentially regulating the anisotropic
654 accumulation of the actomyosin network locally at junctions, facilitating correct apical
655 constriction during ingression (Figure 7E). Our work reveals that pulsed ratchet-like
656 constriction behaviors observed in different species and distinct contexts are conserved
657 in the mouse gastrulation EMT.

658

659

660

661 **METHODS**

662

663 **Experimental animals**

664 FVB or mixed background mice were used for immunofluorescence staining. Most other
665 experiments, incorporating genetically engineered mouse models, were carried out in a
666 mixed background. The *Gt(ROSA)26Sor*$^{tm4(ACTB\text{-}tdTomato,\text{-}EGFP)Luo}$/J (Muzumdar et al.,
667 2007) (referred to throughout as mT/mG) line was obtained from the Jackson
668 Laboratory and crossed to Sox2-Cre (Hayashi et al., 2002) mice to generate a
669 membrane-GFP reporter. The ZO-1-GFP protein fusion knock-in mouse reporter a gift
670 from Terry Lechler (Duke University Medical Center, NC, USA) (Foote et al., 2013;
671 Huebner et al., 2014). *Crumbs2*$^{+/-}$ animals were generated from animals carrying a
672 conditional allele of Crumbs2 via germline deletion (Alves et al., 2013). Animals were
673 housed and bred in accordance with institutional IACUC guidelines. The MSKCC
674 IACUC approved all experiments.

675

676 **Embryo dissection, immunostaining and antibodies**

677 For the majority of immunostaining experiments, embryonic day E7.5 and E8.0 embryos
678 were dissected in cold PBS and fixed for 1 hour in 4% PFA, with the exception that 8%
679 PFA was used for detection of phosphorylated myosin. Whole-mount embryos were
680 blocked overnight in blocking buffer (PBS; 0,1%Triton; 3%BSA), incubated overnight at

681 4°C with primary antibodies, washed in blocking buffer and incubated overnight at 4°C
682 with species-specific secondary antibodies. For staining of F-actin embryos were
683 incubated with Phalloidin-FITC/TRITC (Invitrogen).
684
685 The following antibodies were used: rabbit anti-Myosin Heavy Chain 2B (1/400, Biolegend
686 909902), mouse anti-Myosin Heavy Chain 2B (1/50, DSHB CMII 23), rabbit anti-pMLC
687 (1/200, Cell Signaling Ser19 3671), mouse anti-pMLC (1/200, Cell Signaling Ser19 3675),
688 rabbit anti-ppMLC (1/200, Cell Signaling Thr18/Ser19 3674), rat anti-ZO-1 (1/50, DSHB
689 R26.4C), mouse anti-ZO-1 (1/200, Invitrogen 33-9100), rabbit anti-ZO-1 (1/200, Zymed
690 61-7300), mouse anti-aPKCλ (1/100, BD bioscience 610207), chick anti-GFP (1/400,
691 Abcam 13970). Rabbit anti-Crumbs2 was a gift from Jane McGlade (Hospital for Sick
692 Children, Toronto, Canada) and was used at 1/50 (Laprise 2006). Rabbit anti-PatJ was a
693 gift from Andre Le Bivic (Developmental Biology Institute of Marseille, France) and was
694 usedc at 1/200 (Lemmers 2002). Rat anti-Rock1 was a gift from Masatoshi Takeichi
695 (RIKEN Center for Developmental Biology, Kobe, Japan) and used at 1/100 (Nishimura
696 and Takeichi 2008). Guinea Pig anti-Celsr1 was a gift from Danelle Devenport (Princeton
697 University, Princeton, USA) and was used at 1/500 (Devenport and Fuchs 2008).
698 Fluorescent secondary antibodies Alexa 488, 568 and 647 from Life Technologies and
699 ThermoFisher were used at 1/500.
700
701 **Fixed embryo epiblast mounting and imaging**
702 Following staining, embryos were microdissected to retain the posterior side containing
703 the primitive streak and mounted on glass slide and coverslipped in Fluoromount-G, with
704 the cavity and apical surface of the epiblast facing the coverslip. Layers of tape were
705 placed on both extremity of the slide to create a slight volume and to avoid extensive
706 compression and flattening of the tissue. The position of the primitive streak was
707 determined to coincide with the posterior midline running from the allantois to the node
708 (two morphologically distinguishable structures), and streak axis was oriented so that the
709 proximo-distal axis was oriented along the vertical axis of the image. Most
710 immunostaining revealed a high concentration of puncta also allowing us to identify the
711 location of the primitive streak after imaging. Embryos were imaged on a Leica SP8 or a

712 Zeiss LSM880 laser point scanning confocal using x40 oil immersion objectives, and
713 images were acquired as Z-stacks with 1µm step.
714
715 **Segmentation and quantification of fixed embryo staining**
716 Confocal images were analyzed using ImageJ. The primitive streak region was located
717 and a maximal intensity projection of a minimal thickness (5-10µm) was generated to
718 observe the apical surface of cells in a selected region of interest at the primitive streak.
719 ZO-1 localization was generally used as an apical junction marker for segmentation.
720
721 Segmentation was performed using the Tissue Analyzer software (Aigouy et al., 2010;
722 Aigouy et al., 2016), an ImageJ plugin which uses a watershed algorithm to segment the
723 cell cortex. Briefly, a first membrane segmentation was automatically performed, and then
724 verified and corrected manually. Cells and junctions were tracked and assigned IDs. Most
725 cell parameters used were calculated by the software, including; apical surface area, cell
726 elongation magnitude and orientation, number of junctions per cell, and signal intensities
727 along junctions. In brief, cell surface elongation is characterized by an axis and
728 magnitude, and can be represented by a symmetric tensor at the centroid of a cell (images
729 with red nematic bars). Calculation integrates cell area and shape so that cells of similar
730 shape with different sizes are assigned the same value of cell elongation (see Aigouy et
731 al. 2016 for details equations (Aigouy et al., 2016)).
732
733 Color-code representations of apical surface area, surface elongation, and junction
734 number were generated in Tissue Analyzer. Surface elongation index (magnitude)
735 calculated by the software, was represented as an index from 0 (round) to 1 (line). Surface
736 elongation and planar polarity of proteins were characterized by an axis and magnitude,
737 represented by a symmetric tensor at the centroid of a cell (images with red nematic bars).
738
739 Intensity measurements of immunostaining are presented for every data as the mean
740 intensity along single junctions and normalized to the global mean junctional intensity of
741 corresponding embryos. Anisotropy parameters were calculated from junctional
742 intensities measured within Tissue Analyzer. Intensities were measured along 3 pixel-

743 wide lines (~500nm), measurements were extracted from a database created by the
744 software and used externally for calculations. For each single cell analyzed, the mean
745 junction intensity was used to calculate per cell, the standard deviation between the
746 intensity of all junctions, and the junction with the maximal intensity divided by the junction
747 with the minimal intensity (Max/Min ratio). These two parameters were used to evaluate
748 the anisotropic accumulation of proteins at apical junctions. Double immunostainings
749 were used to assess correlative accumulation of proteins, and mean junction intensities
750 were used to create scatter plots to evaluate the dispersion of the intensity across the
751 populations, and their correlation coefficients. Generally, measurements taken of
752 junctions from different embryos were pooled, except for a few examples in which
753 junctions were grouped by individual cells to evaluate the range of anisotropy in different
754 cells.
755
756 For planar polarity of protein localization at apical junctions, Tissue Analyzer calculates a
757 planar polarity characterized by an axis and magnitude, and can be represented by a
758 symmetric tensor at the centroid of a cell (images with red nematic bars). Cell junctions
759 fluorescent intensity as well as the angles of junction and the geometry of the cell were
760 used to define the magnitude of polarity as well as the angle (see Aigouy et al. 2016 for
761 details equations (Aigouy et al., 2016)). For protein accumulation based on junctional
762 orientation, average junctional intensities were plotted according to junctional orientation
763 angles which were classified in bins of 15°.
764
765 For protein quantifications in *Crb2*$^{-/-}$ mutants and comparison with wild-type (WT)
766 embryos, 3-4 embryos of each genotype recovered from 2-3 litters where processed,
767 immunostained and imaged in parallel using the same parameters, then segmented and
768 quantified as described above. Measurements are presented as the mean intensity along
769 single junctions and normalized to the global mean junctional intensity of the pool cohort
770 of embryos of both genotypes for each proteins.
771
772 **Time-lapse imaging**

773 For time lapse imaging, mid- to late-streak stage embryos (E7.5) were dissected with their
774 yolk sac and ectoplacental cone intact in dissection medium (CO_2 independent DMEM,
775 10%FBS) at 37°C. Embryos were stabilized in a depression created in a layer of collagen
776 matrix and imaged in glass-bottom 35mm MatTek dishes. They were placed with their
777 posterior side facing the objective and culture in 50% rat serum/50% DMEM media in an
778 incubation chamber at 37°C and 5% CO_2. Embryos were imaged for a total of 3-6h with
779 Z-stacks of 1µm step acquired every 5min (minimum time-scale possible to keep embryo
780 and fluorescent signal integrity) on a Leica-SP8 laser point scanning confocal or a Nikon
781 A1RHD25 high speed resonant scanning confocal with 40x objectives. Imaging usually
782 focused on regions of interest in the proximo-distal middle of the primitive steak where
783 the epiblast is the least curved and optimal for image data acquisition and analysis.
784
785 **Dynamic images analysis and quantification**
786 Membrane-GFP from *mT/mG* embryos was used to observed apical constriction
787 associated with cell ingression at the primitive streak. For all other imaging and
788 quantification, a ZO-1-GFP Knock-in reporter was used as it generally gave the best
789 signal-to-noise enabling observation of apical surfaces of epiblast cells. Analyses were
790 performed in ImageJ and Tissue Analyzer on maximal projections of Z-stacks. Cell
791 tracking in the plane of the epithelium was performed manually using the Manual Tracking
792 plugin in ImageJ. To quantify ingression events, small areas of interest in the vicinity of
793 the primitive streak, corresponding to a ~40µm region along the predicted midline, were
794 analyzed. All cells were tracked for at least one hour, and constriction and ingression
795 events were identified to calculate the ratio of ingression events per hour. Ingression
796 events were considered isolated when the constriction and disappearance of a cell
797 occurred within 30min or more of the ingression of adjacent neighboring cells, and
798 clustered when occurring within a 30min window of the ingression of adjacent neighboring
799 cells (2-4 cells in different clustered events).
800
801 For dynamic analysis of apical surfaces, small regions of interest at the primitive streak
802 were used for segmentation with Tissue analyzer. A first segmentation was automatically
803 generated by the software, then each time-point manually corrected. Cell parameters,

804 including apical surface area, surface elongation index and orientation and number of
805 edges, were extracted from the segmentation database, and graphs were plotted using
806 GraphPad Prism.
807
808 The beginning of cell constriction associated with an ingression event was defined as the
809 point when cells started to reduce their apical surface area after a period of oscillation,
810 and so continually until they completely lost their apical domain. The start of constriction
811 was defined as t0 when the apical surface area, rate of change of surface area and other
812 parameters were plotted against time. Changes in apical surface area (constriction rate)
813 was defined as the inverse value of the derivative of apical surface area: Δarea(t)=area(t-
814 1) – area(t). Oscillations of surface area in epiblast cells away from the primitive streak,
815 and before the initiation of ingression were compared with the more dramatic changes in
816 surface area during the constriction period. During ingression, a constriction pulse was
817 defined as an event in which the contraction rate exceeded one standard deviation above
818 the mean of the contraction rate of non-ingressing cells (above 0.7 μm^2/min). The number
819 of pulses, occurrence of pulse and pulse magnitude were quantified manually for each
820 constriction period of each cell and each pulse. The calculated apical area rate of change
821 was integrated in the Tissue Analyzer database, and used to generate color-coded movie
822 representations of surface area, area rate of changes, cell elongation, number of junctions
823 and junction length. As for fixed embryo analysis, surface elongation index (magnitude)
824 calculated by the software, is represented as an index from 0 (round) to 1 (line). Surface
825 elongation is characterized by an axis and magnitude, and is represented by a symmetric
826 tensor at the centroid of a cell (red nematic bars).
827
828 Changes in junction length (shrinkage rate) was defined similarly to cell area changes, as
829 the inverse value of the derivative of junction length: Δlength(t)=length(t-1) – length(t). To
830 analyze and compare junctions length changes over time, correlation of pairs of junctions
831 were quantified and plot as correlation matrix to illustrate a single cell or correlation
832 coefficient plot for pool of single cells. The average shrinkage rate of single junctions
833 during consecutive cell constriction pulses and stable phases were calculated to visualize
834 the asynchronous and differential shrinkage of junctions during single cell constriction.

835

836 **Statistics**

837 A minimum of 3 embryos were analyzed for each experiment (samples sizes are detailed
838 in Figure legends). Error bars on graphs represent s.e.m. P values corresponds to an
839 unpaired non-parametric Mann-Whitney test.

840

841 **Definition of terms**

842 Start of constriction: the beginning of cell constriction associated with an ingression event
843 at the primitive streak was defined as the time point when cells started to reduce their
844 apical surface area after a period of oscillation, and so continually until they completely
845 lost their apical domain.

846 End of constriction: the end of constriction was defined as the time point when the
847 constricting cells lost their apical surface and move out of the plan of the epiblast.

848 Before constriction: defines the time period before cells start their constriction at the
849 primitive streak. This time-period shows same oscillation characteristics of the apical
850 surface area as epiblast cells further away from the primitive streak.

851 Constriction: defines the time-period during which cells reduced their apical surface area
852 until they completely lose their apical domain. We also use the term for the constriction
853 rate and constriction pulse.

854 Contraction/expansion: used to define the rate of change in apical surface area through
855 time, contraction defining the rate of reduction in area, and expansion a rate of increase
856 in area. They are defined both as positive value and plotted as rate of change, or in some
857 cases defined negatively and positively and plotted as constriction rate.

858 Constriction pulse: defines the time-period during the constriction when the rate of
859 contraction of the apical surface area exceeds the threshold.

860 Stable phases: defines the time-period between constriction pulses, when the change in
861 apical surface area shows minimal variation.

862 Pulse occurrence: defines the frequency at which constriction pulses are occurring.

863 Pulse magnitude: defines as the maximum value of constriction rate within each pulse.

864 Shrinkage: defines the junction reduction in length, Shrinkage rate indicates the change
865 in junction length through time.

Acknowledgements

AF and AKH dedicate this manuscript to the memory of our late colleague and mentor Kathryn V Anderson. Kathryn marveled at the spectacle of mammalian gastrulation and recognized the insights that genetics and imaging would bring. We thank Andre Le Bivic for the PatJ antibody, Danelle Devenport for the Celsr1 antibody, Jane McGlade for the Crumbs2 antibody and Masatoshi Takeichi for the Rock1 antibody. We thank Terry Lechler for the ZO-1-GFP animals. We thank Zhirong Bao, Alex Joyner, Jen Zallen and members of the Hadjantonakis lab for stimulating discussions and critical feedback on the work. We thank the MSKCC (Memorial Sloan Kettering Cancer Center) Molecular Cytology, and the SKI Light Microscopy Instrument Cluster and James Muller for imaging technical support. This study was supported by the NIH (R01HD094868, R01DK127821, R01HD086478, and P30CA008748). AF was supported by a postdoctoral fellowship from the MSKCC GMTEC (The Alan and Sandra Gerry Metastasis and Tumor Ecosystems Center) for part of this work.

882 Aigouy, B., R. Farhadifar, D.B. Staple, A. Sagner, J.C. Roper, F. Julicher, and S. Eaton. 2010. Cell
883 flow reorients the axis of planar polarity in the wing epithelium of Drosophila. *Cell*.
884 142:773-786.

885 Aigouy, B., D. Umetsu, and S. Eaton. 2016. Segmentation and Quantitative Analysis of Epithelial
886 Tissues. *Methods Mol Biol*. 1478:227-239.

887 Alves, C.H., A.S. Sanz, B. Park, L.P. Pellissier, N. Tanimoto, S.C. Beck, G. Huber, M. Murtaza, F.
888 Richard, I. Sridevi Gurubaran, M. Garcia Garrido, C.N. Levelt, P. Rashbass, A. Le Bivic, M.W.
889 Seeliger, and J. Wijnholds. 2013. Loss of CRB2 in the mouse retina mimics human retinitis
890 pigmentosa due to mutations in the CRB1 gene. *Hum Mol Genet*. 22:35-50.

891 An, Y., G. Xue, Y. Shaobo, D. Mingxi, X. Zhou, W. Yu, T. Ishibashi, L. Zhang, and Y. Yan. 2017. Apical
892 constriction is driven by a pulsatile apical myosin network in delaminating Drosophila
893 neuroblasts. *Development*. 144:2153-2164.

894 Biehler, C., K.E. Rothenberg, A. Jette, H.M. Gaude, R. Fernandez-Gonzalez, and P. Laprise. 2021.
895 Pak1 and PP2A antagonize aPKC function to support cortical tension induced by the
896 Crumbs-Yurt complex. *Elife*. 10.

897 Christodoulou, N., and P.A. Skourides. 2015. Cell-Autonomous Ca(2+) Flashes Elicit Pulsed
898 Contractions of an Apical Actin Network to Drive Apical Constriction during Neural Tube
899 Closure. *Cell Rep*. 13:2189-2202.

900 Chuai, M., W. Zeng, X. Yang, V. Boychenko, J.A. Glazier, and C.J. Weijer. 2006. Cell movement
901 during chick primitive streak formation. *Dev Biol*. 296:137-149.

902 Chung, S., S. Kim, and D.J. Andrew. 2017. Uncoupling apical constriction from tissue invagination.
903 *Elife*. 6.

904 Coravos, J.S., and A.C. Martin. 2016. Apical Sarcomere-like Actomyosin Contracts Nonmuscle
905 Drosophila Epithelial Cells. *Dev Cell*. 39:346-358.

906 Coravos, J.S., F.M. Mason, and A.C. Martin. 2017. Actomyosin Pulsing in Tissue Integrity
907 Maintenance during Morphogenesis. *Trends Cell Biol*. 27:276-283.

908 Curtin, J.A., E. Quint, V. Tsipouri, R.M. Arkell, B. Cattanach, A.J. Copp, D.J. Henderson, N. Spurr, P.
909 Stanier, E.M. Fisher, P.M. Nolan, K.P. Steel, S.D. Brown, I.C. Gray, and J.N. Murdoch. 2003.
910 Mutation of Celsr1 disrupts planar polarity of inner ear hair cells and causes severe neural
911 tube defects in the mouse. *Curr Biol*. 13:1129-1133.

912 Ferrer-Vaquer, A., M. Viotti, and A.K. Hadjantonakis. 2010. Transitions between epithelial and
913 mesenchymal states and the morphogenesis of the early mouse embryo. *Cell Adh Migr*.
914 4:447-457.

915 Foote, H.P., K.D. Sumigray, and T. Lechler. 2013. FRAP analysis reveals stabilization of adhesion
916 structures in the epidermis compared to cultured keratinocytes. *PLoS One*. 8:e71491.

917 Francou, A., and K.V. Anderson. 2020. The Epithelial-to-Mesenchymal Transition (EMT) in
918 Development and Cancer. *Annu Rev Cancer Biol*. 4:197-220.

919 Hayashi, S., P. Lewis, L. Pevny, and A.P. McMahon. 2002. Efficient gene modulation in mouse
920 epiblast using a Sox2Cre transgenic mouse strain. *Mech Dev*. 119 Suppl 1:S97-S101.

921 Heer, N.C., and A.C. Martin. 2017. Tension, contraction and tissue morphogenesis. *Development*.
922 144:4249-4260.

923 Huebner, R.J., T. Lechler, and A.J. Ewald. 2014. Developmental stratification of the mammary
924 epithelium occurs through symmetry-breaking vertical divisions of apically positioned
925 luminal cells. *Development*. 141:1085-1094.

926 Ishiuchi, T., and M. Takeichi. 2011. Willin and Par3 cooperatively regulate epithelial apical
927 constriction through aPKC-mediated ROCK phosphorylation. *Nat Cell Biol*. 13:860-866.

928 Lecuit, T., and P.F. Lenne. 2007. Cell surface mechanics and the control of cell shape, tissue
929 patterns and morphogenesis. *Nat Rev Mol Cell Biol*. 8:633-644.

930 Lim, J., and J.P. Thiery. 2012. Epithelial-mesenchymal transitions: insights from development.
931 *Development*. 139:3471-3486.

932 Mahaffey, J.P., J. Grego-Bessa, K.F. Liem, Jr., and K.V. Anderson. 2013. Cofilin and Vangl2
933 cooperate in the initiation of planar cell polarity in the mouse embryo. *Development*.
934 140:1262-1271.

935 Marston, D.J., C.D. Higgins, K.A. Peters, T.D. Cupp, D.J. Dickinson, A.M. Pani, R.P. Moore, A.H. Cox,
936 D.P. Kiehart, and B. Goldstein. 2016. MRCK-1 Drives Apical Constriction in C. elegans by
937 Linking Developmental Patterning to Force Generation. *Curr Biol*. 26:2079-2089.

938 Martin, A.C., and B. Goldstein. 2014. Apical constriction: themes and variations on a cellular
939 mechanism driving morphogenesis. *Development*. 141:1987-1998.

940 Martin, A.C., M. Kaschube, and E.F. Wieschaus. 2009. Pulsed contractions of an actin-myosin
941 network drive apical constriction. *Nature*. 457:495-499.

942 Mason, F.M., M. Tworoger, and A.C. Martin. 2013. Apical domain polarization localizes actin-
943 myosin activity to drive ratchet-like apical constriction. *Nat Cell Biol*. 15:926-936.

944 Mathiah, N., E. Despin-Guitard, M. Stower, W. Nahaboo, E.S. Eski, S.P. Singh, S. Srinivas, and I.
945 Migeotte. 2020. Asymmetry in the frequency and position of mitosis in the mouse embryo
946 epiblast at gastrulation. *EMBO Rep*. 21:e50944.

947 McDole, K., L. Guignard, F. Amat, A. Berger, G. Malandain, L.A. Royer, S.C. Turaga, K. Branson,
948 and P.J. Keller. 2018. In Toto Imaging and Reconstruction of Post-Implantation Mouse
949 Development at the Single-Cell Level. *Cell*. 175:859-876 e833.

950 Morgani, S.M., and A.K. Hadjantonakis. 2020. Signaling regulation during gastrulation: Insights
951 from mouse embryos and in vitro systems. *Curr Top Dev Biol*. 137:391-431.

952 Muzumdar, M.D., B. Tasic, K. Miyamichi, L. Li, and L. Luo. 2007. A global double-fluorescent Cre
953 reporter mouse. *Genesis*. 45:593-605.

954 Nakaya, Y., and G. Sheng. 2008. Epithelial to mesenchymal transition during gastrulation: an
955 embryological view. *Dev Growth Differ*. 50:755-766.

956 Nishimura, T., H. Honda, and M. Takeichi. 2012. Planar cell polarity links axes of spatial dynamics
957 in neural-tube closure. *Cell*. 149:1084-1097.

958 Petrov, D., I. Dahan, E. Cohen-Kfir, and S. Ravid. 2017. aPKCzeta affects directed cell migration
959 through the regulation of myosin light chain phosphorylation. *Cell Adh Migr*. 11:347-359.

960 Ramkumar, N., and K.V. Anderson. 2011. SnapShot: mouse primitive streak. *Cell*. 146:488-488
961 e482.

962 Ramkumar, N., T. Omelchenko, N.F. Silva-Gagliardi, C.J. McGlade, J. Wijnholds, and K.V.
963 Anderson. 2016. Crumbs2 promotes cell ingression during the epithelial-to-mesenchymal
964 transition at gastrulation. *Nat Cell Biol*. 18:1281-1291.

965 Roh-Johnson, M., G. Shemer, C.D. Higgins, J.H. McClellan, A.D. Werts, U.S. Tulu, L. Gao, E. Betzig,
966 D.P. Kiehart, and B. Goldstein. 2012. Triggering a cell shape change by exploiting
967 preexisting actomyosin contractions. *Science*. 335:1232-1235.

968 Roper, K. 2012. Anisotropy of Crumbs and aPKC drives myosin cable assembly during tube
969 formation. *Dev Cell*. 23:939-953.

970 Rozbicki, E., M. Chuai, A.I. Karjalainen, F. Song, H.M. Sang, R. Martin, H.J. Knolker, M.P.
971 MacDonald, and C.J. Weijer. 2015. Myosin-II-mediated cell shape changes and cell
972 intercalation contribute to primitive streak formation. *Nat Cell Biol*. 17:397-408.

973 Samarage, C.R., M.D. White, Y.D. Alvarez, J.C. Fierro-Gonzalez, Y. Henon, E.C. Jesudason, S.
974 Bissiere, A. Fouras, and N. Plachta. 2015. Cortical Tension Allocates the First Inner Cells of
975 the Mammalian Embryo. *Dev Cell*. 34:435-447.

976 Serrano Najera, G., and C.J. Weijer. 2020. Cellular processes driving gastrulation in the avian
977 embryo. *Mech Dev*. 163:103624.

978 Sidor, C., T.J. Stevens, L. Jin, J. Boulanger, and K. Roper. 2020. Rho-Kinase Planar Polarization at
979 Tissue Boundaries Depends on Phospho-regulation of Membrane Residence Time. *Dev*
980 *Cell*. 52:364-378 e367.

981 Simoes, S., G. Lerchbaumer, M. Pellikka, P. Giannatou, T. Lam, D. Kim, J. Yu, D. Ter Stal, K. Al
982 Kakouni, R. Fernandez-Gonzalez, and U. Tepass. 2022. Crumbs complex-directed apical
983 membrane dynamics in epithelial cell ingression. *J Cell Biol*. 221.

984 Simoes, S., Y. Oh, M.F.Z. Wang, R. Fernandez-Gonzalez, and U. Tepass. 2017. Myosin II promotes
985 the anisotropic loss of the apical domain during Drosophila neuroblast ingression. *J Cell*
986 *Biol*. 216:1387-1404.

987 Thiery, J.P. 2002. Epithelial-mesenchymal transitions in tumour progression. *Nat Rev Cancer*.
988 2:442-454.

989 Thiery, J.P., H. Acloque, R.Y. Huang, and M.A. Nieto. 2009. Epithelial-mesenchymal transitions in
990 development and disease. *Cell*. 139:871-890.

991 Voiculescu, O., F. Bertocchini, L. Wolpert, R.E. Keller, and C.D. Stern. 2007. The amniote primitive
992 streak is defined by epithelial cell intercalation before gastrulation. *Nature*. 449:1049-
993 1052.

994 Voiculescu, O., L. Bodenstein, I.J. Lau, and C.D. Stern. 2014. Local cell interactions and self-
995 amplifying individual cell ingression drive amniote gastrulation. *Elife*. 3:e01817.

996 Williams, M., C. Burdsal, A. Periasamy, M. Lewandoski, and A. Sutherland. 2012. Mouse primitive
997 streak forms in situ by initiation of epithelial to mesenchymal transition without migration
998 of a cell population. *Dev Dyn*. 241:270-283.

999 Ye, X., and R.A. Weinberg. 2015. Epithelial-Mesenchymal Plasticity: A Central Regulator of Cancer
1000 Progression. *Trends Cell Biol*. 25:675-686.
1001

1002

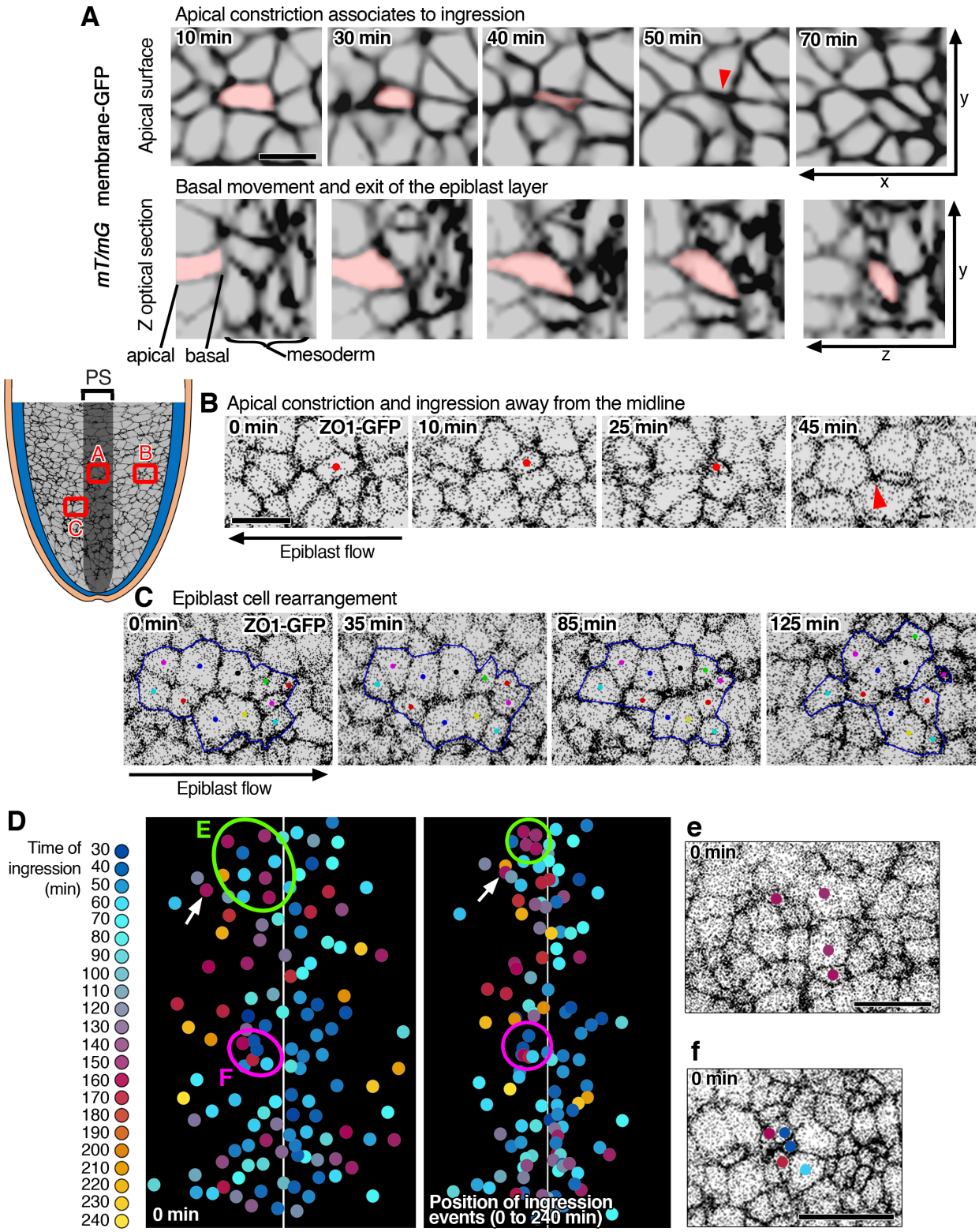

Figure 1-figure supplement 1: Apical constriction and ingression of epiblast cells in the vicinity of the mouse primitive streak. **(A)** Snapshots of a time-lapse of membrane-GFP in an *mTmG* embryo showing apical surface constriction in a single Z plan below the apical membrane (top

row) associated to ingression out of the epiblast layer and integration to the mesoderm seen on apicobasal Z optical section (bottom row) at the primitive streak (region located on the schematic). **(B)** Example of cell constricting away from the midline, as the epiblast cells move toward the primitive streak. **(C)** Example showing cell rearrangement among a cluster of epiblast cells near the primitive streak. **(D)** Color-coded time-series and position of ingression events of tracked cells shown in Figure 1d,e. The initial position of a circled group of cells (green circle) is shown in e; cells are not all neighbors at 0min but ingress together as neighbors (after 165min). Another group of cells (purple circle) who's initial position is shown in f; cells are neighbors at 0min, but they do not ingress at the same time. Cells are considered to constrict and ingress as isolated cells when their ingression takes place 30min or more from their neighbors. White arrow shows the ingression of an isolated cell.
Scale bars A,B,C 10μm; E,F 20μm.

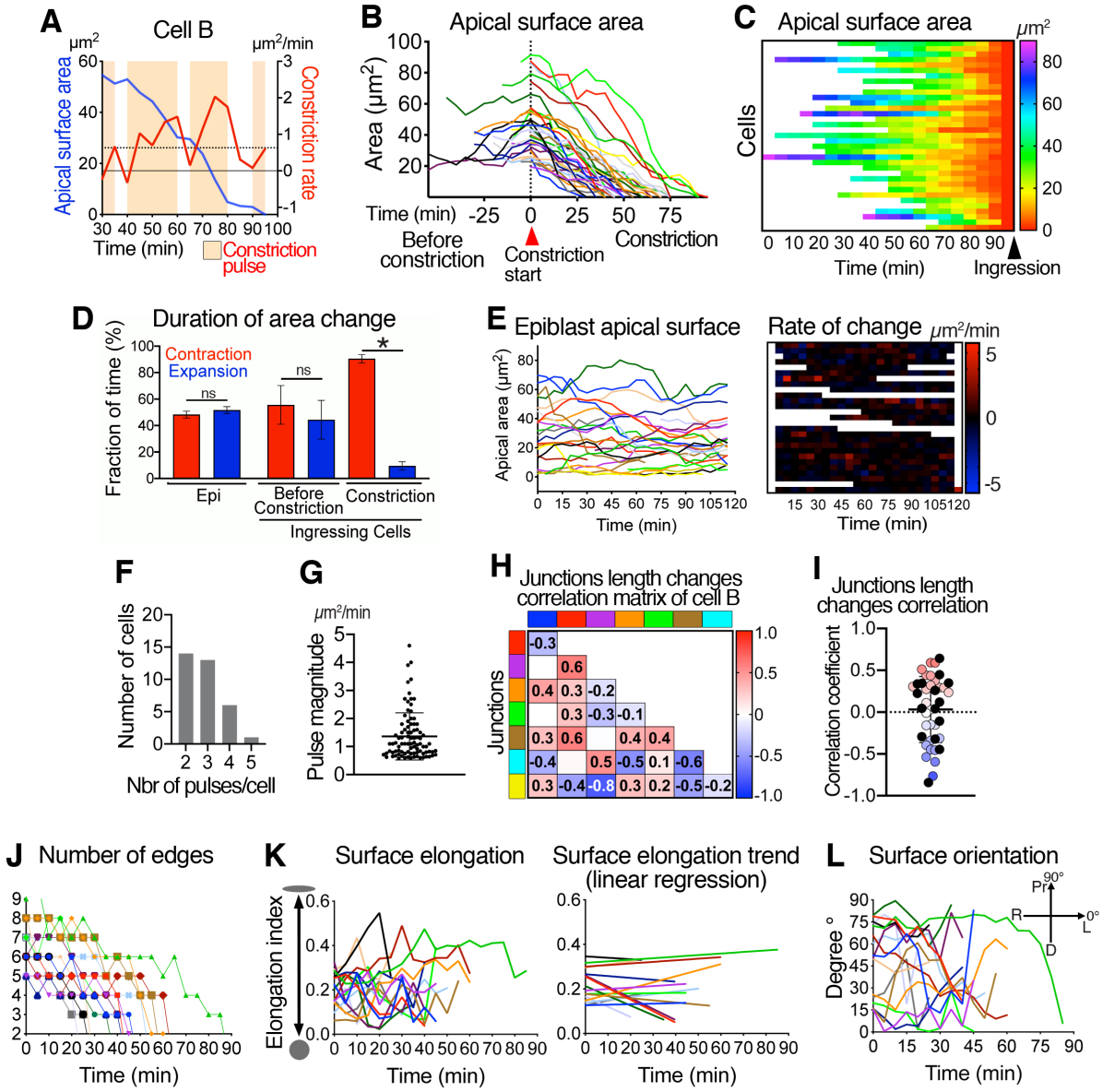

Figure 2,3-figure supplement 1: Details and features of constriction pulses and cell parameters during constriction. **(A)** Graph of apical surface area and rate of constriction of single cell B (shown in Figure 3D,E) exhibiting four pulses of constriction (beige regions). **(B)** Plot showing the apical surface area of several cells at the primitive streak during the total time of the analysis. 0min marks the beginning of the constriction period. Cells begin with a wide range of different initial apical surfaces prior to their constriction. **(C)** Heat map plot of the apical surface area during constriction showing the reduction in area and the pulses of constriction. Each row represents data for an individual cell. **(D)** Fraction of time cells spend contracting or expending their apical surfaces revealing equilibrium in lateral epiblast and at the streak before the constriction period, followed by significantly longer contraction time during constriction. **(E)**

1032 Plot showing the apical surface area and heat map color-code of rate of change of epiblast cells
1033 outside the region occupied by the primitive streak before ingression. Cells exhibit a wide variety
1034 of apical areas, and fluctuate their apical surfaces, with a low rate of contraction and expansion
1035 through time. (Corresponding measurements are shown in D and Figure 2E). **(F)** Frequency
1036 distribution graph showing the proportion of cells undergoing two to four main constriction
1037 pulses. **(G)** Dot plot showing the average magnitude of constriction pulses. **(H)** Matrix heat map
1038 showing the correlation of junction length changes through time of cell B shown in a and 2i,j.
1039 Some junctions show correlation and change their length during the same time when others
1040 show anti-correlation. Each row and column represent a single junction and are color-coded as
1041 in a and 2I,J. Numbers represent the correlation coefficients of each pairs of junction compared.
1042 **(I)** Dot plot showing the correlation coefficients of junction length changes through time of
1043 junctions from multiple cells. Correlation of junctions shown in H are colored. **(J)** Plot showing
1044 the number of edges during the constriction period. Cells have different initial numbers of edges,
1045 and gradually lose them during the constriction period. **(K)** Plot showing the apical surface
1046 elongation index calculated by Tissue Analyzer, from 0 to 1, with 0 being perfectly round, and 1
1047 corresponding to a line. Cells show fluctuation in their elongation during constriction, but exhibit
1048 no significant trend (trend showed by the linear regressions). **(L)** Plot showing apical surface
1049 orientation in the plane of the epiblast epithelial layer. Cells show fluctuation of orientation axis
1050 during constriction, and do not show significant pattern of elongation.
1051 51 cells quantified from 4 embryos. *$P<0.05$ (Unpaired bilateral Mann-Whitney test). Error bars
1052 represent s.e.m. Scale bar, 10μm
1053
1054

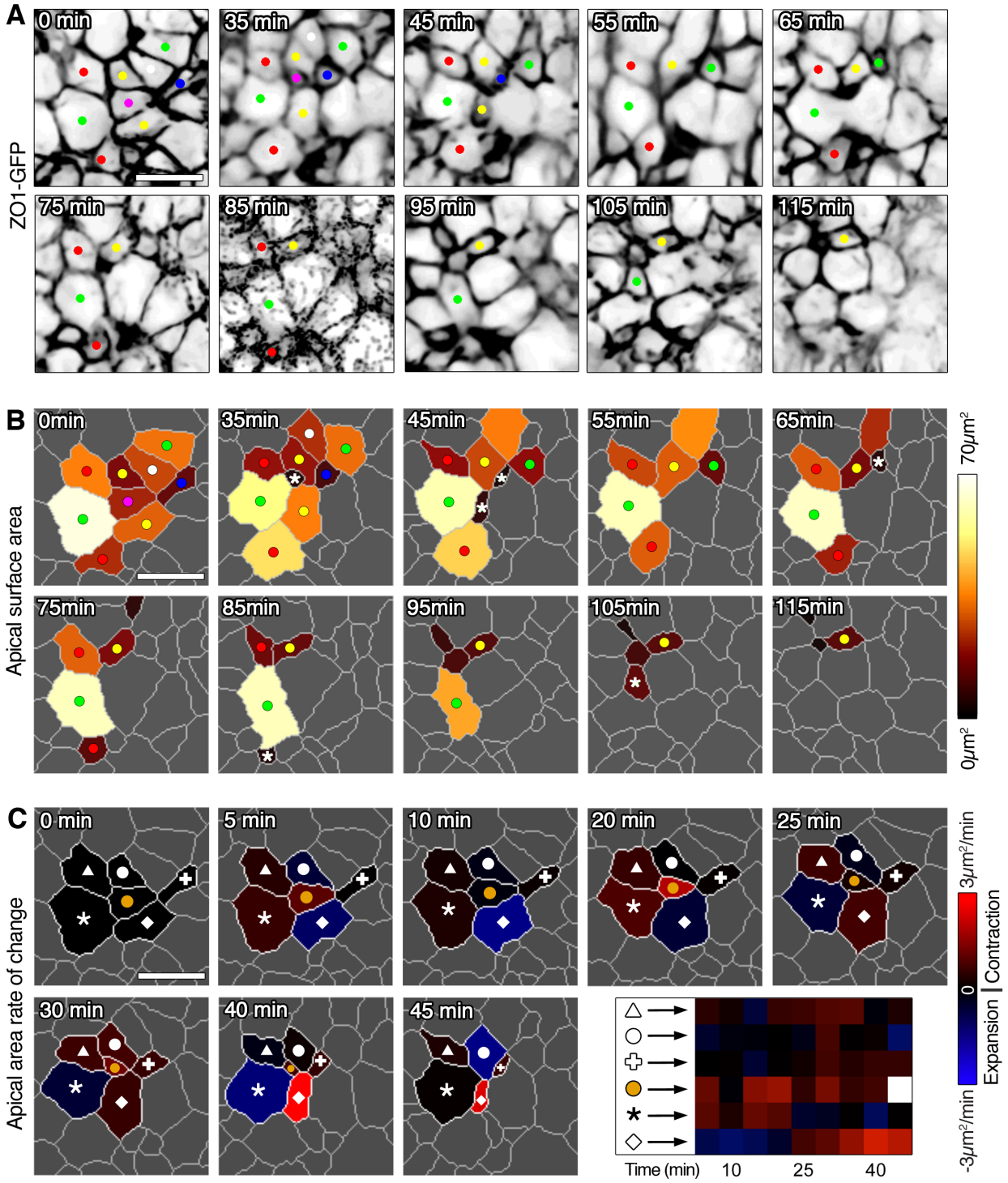

Figure 2-figure supplement 2: Asynchronous apical constriction at the multi-cellular level. **(A)** Time-series of ZO-1-GFP reporter expression identifying a cluster of epiblast cells exhibiting apparent stochastic apical constriction and cell ingression. **(B)** Membrane segmentation and color-coded time-series of apical surface area showing oscillation in apical surfaces in the cell

1060 cluster and asynchronous reduction of apical surfaces during ingression (asterisks). **(C)** Color-
1061 coded time-series and heat map plot of rate of change of apical surface area showing
1062 asynchronous oscillation in area and asynchronous constriction. Note that as one cell in the
1063 middle constricts and ingresses (orange dot), neighboring cells asynchronously change their
1064 apical surfaces; some will constrict and ingress shortly after, while others will only ingress at a
1065 later time point. Each row represents data for an individual cell. Scale bars, 10μm
1066

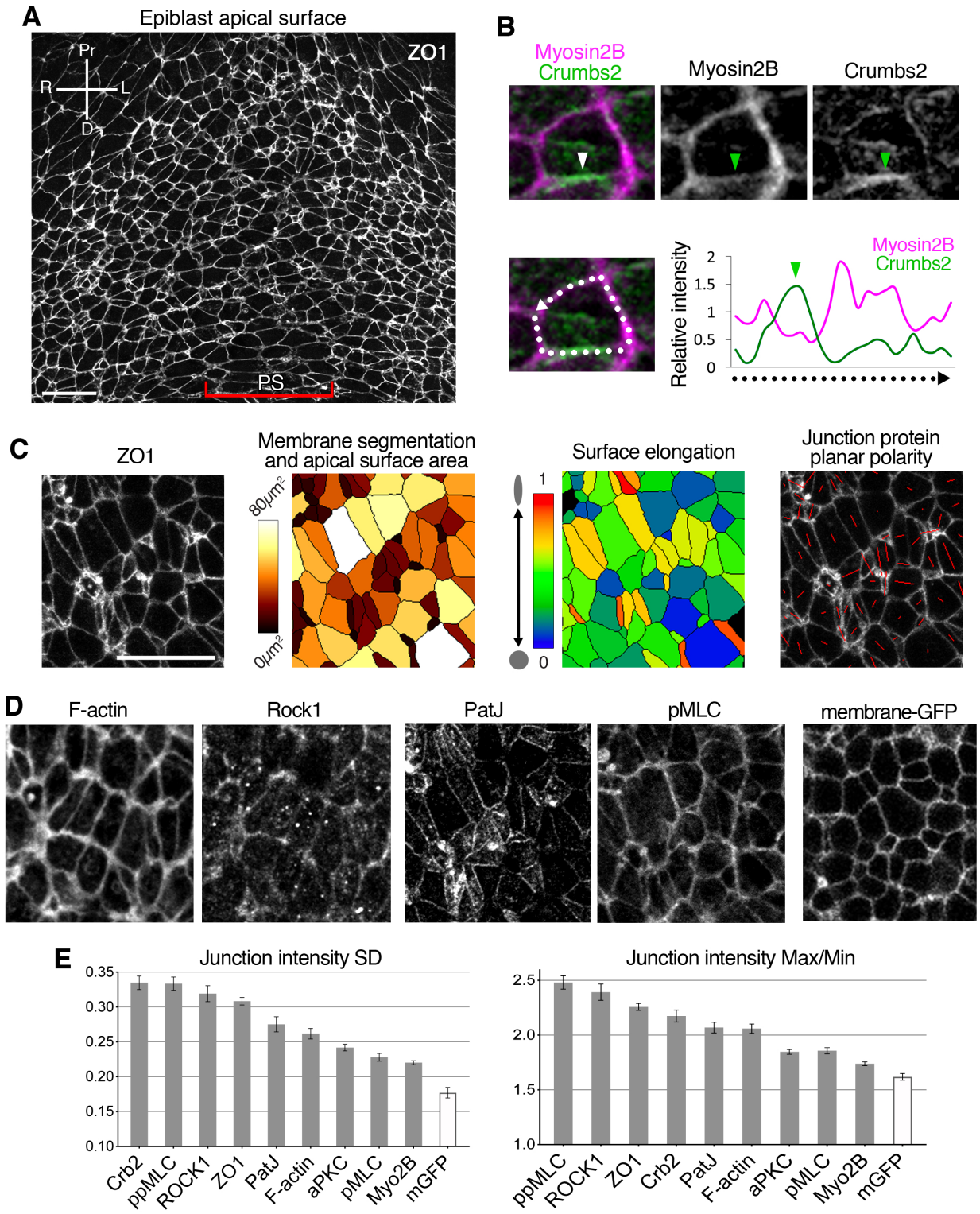

Figure 4-figure supplement 1: Complementary accumulation of Crumbs2 and Myosin2B, and anisotropy of apical components at the primitive streak. **(A)** ZO-1 immunostaining on fixed E7.5 embryo showing the apical surface of epiblast cells in the posterior. **(B)** High magnification view

1071 of a single cell stained for Myosin2B (magenta) and Crumbs2 (green) showing strong Crumbs2
1072 accumulation on one junction (arrowhead) and predominant Myosin accumulation on other
1073 junctions. White dashed line and arrow indicate the membrane intensity measurement shown in
1074 the plot. The junction with the highest level of Crumbs2 (arrowhead) has the lowest level of
1075 Myosin, whereas Myosin predominates (and Crumbs is reduced) at the rest of the junctions. **(C)**
1076 ZO-1 immunostaining used for cell apical membrane identification and segmentation, allows
1077 quantification of junctional intensity of staining, and determination of a number of parameters,
1078 including apical surface area, surface elongation and protein planar polarity. **(D)** Staining F-
1079 actin, Rock1, PatJ and pMLC exhibiting different patterns of accumulation at apical cell-cell
1080 junctions, and a membrane-GFP reporter more homogeneously present at the apical
1081 membrane. **(E)** Plots of anisotropy parameters, junctional Standard Deviation and Max/Min.
1082 Proteins exhibit a range of distributions and anisotropy levels, some like Crumbs2 and ppMLC
1083 show a high level of anisotropy, others like PatJ and F-Actin show moderate anisotropy, and
1084 some like aPKC pMLC and Myosin2B show a lower level of anisotropy closer to the level of the
1085 negative control membrane-GFP. Error bars represent s.e.m.
1086

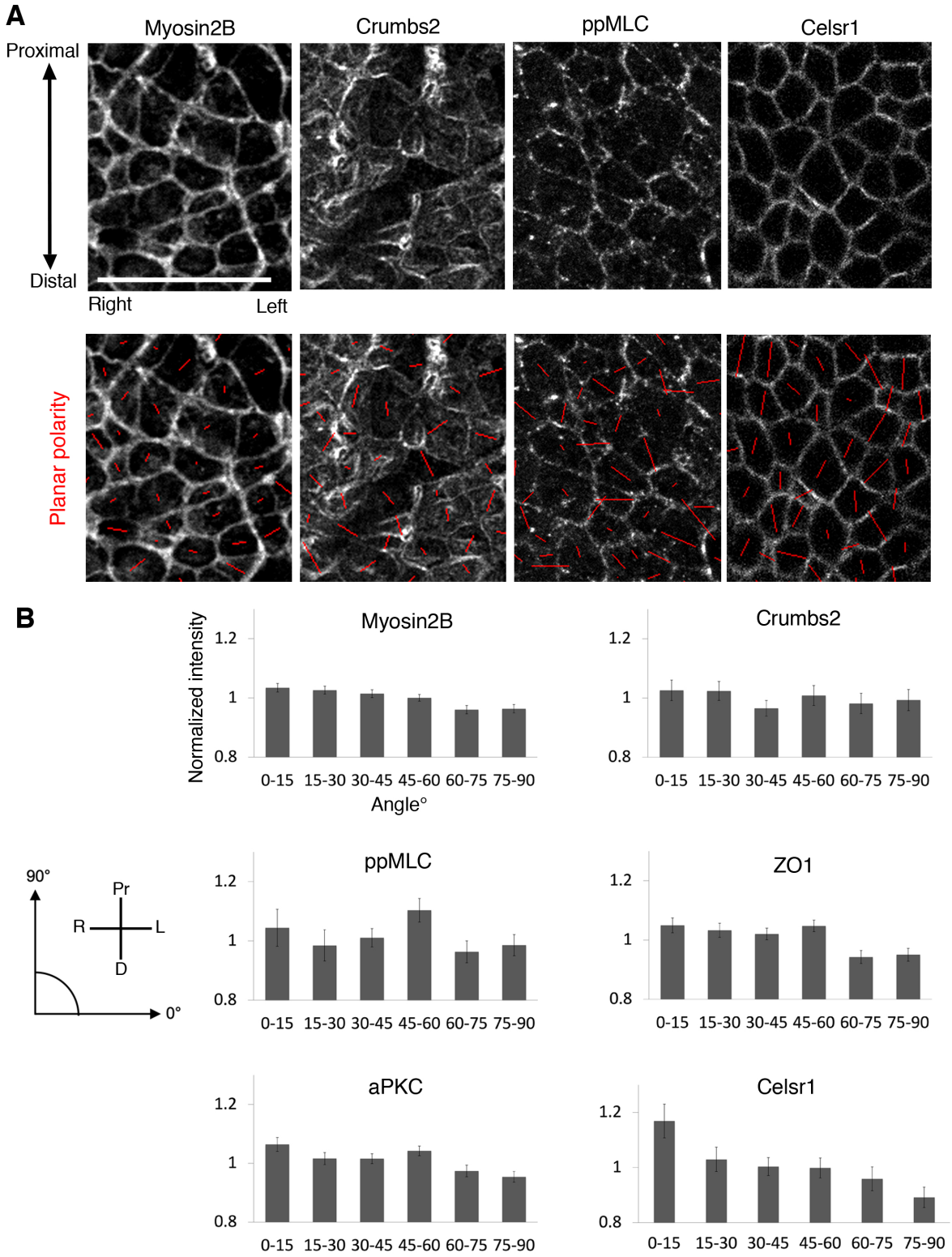

Figure 4-figure supplement 2: Apical proteins show anisotropy accumulation but no planar polarity. **(A)** Immunostaining for Myosin2B, Crumbs2, ppMLC and Celsr1 with associated polarity visualization (red tensor) calculated after membrane segmentation, showing the

1091 orientation (orientation of the tensor) and amplitude of polarity (length of the tensor). **(B)**
1092 Junctional protein intensity plotted as a function of junctional angle. 0° is parallel to the left/right
1093 axis and 90° is parallel to the proximal/distal axis.
1094 The apical proteins described previously and measured here (Myosin2B, Crumbs2, ppMLC, ZO-
1095 1 and aPKC) do not show planar polarity, red bars in A showing polarity of intensity are not
1096 oriented in specific axis, and intensity in B show no bias at a particular angle. By contrast, the
1097 PCP protein Celsr1 exhibits evident polarity, red bars tend to be vertically oriented, and intensity
1098 in B shows a significant increase in Celsr1 levels at edges oriented parallel to the left/right axis.
1099 Celsr1 preferentially accumulates at horizontal junctions (left-right embryo orientation). Error
1100 bars represent s.e.m.
1101

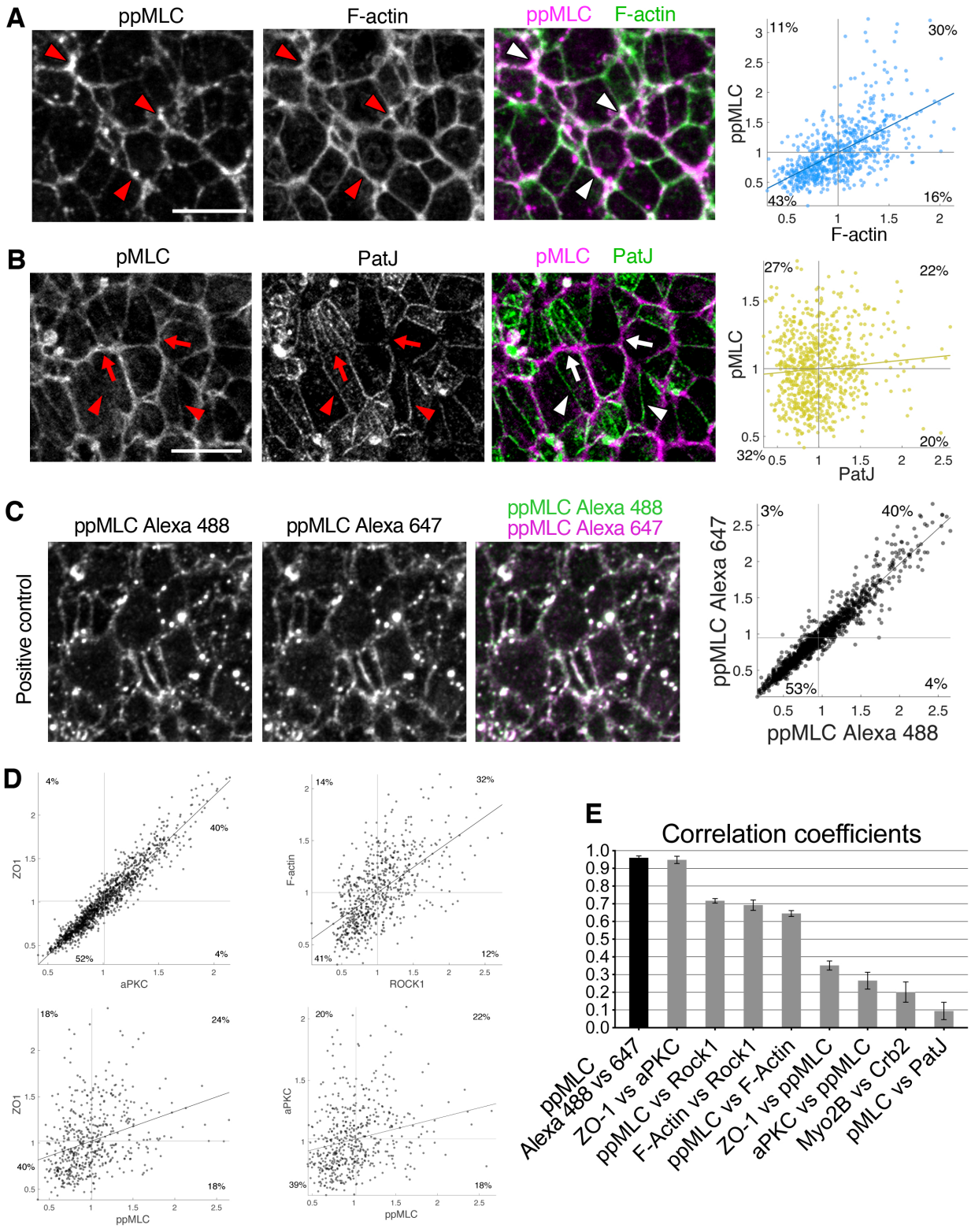

Figure 5-figure supplement 1: Correlation of protein distributions at apical junctions. **(A)** Co-immunostaining of ppMLC and F-Actin reveals a tendency to accumulate on the same junctions. Note colocalization of fluorescent signal on most junctions (arrowheads). Scatter plot on the

1106 right showing elevated intensity correlation of the two proteins. Each point represented the
1107 mean intensity at a single junction. **(B)** Co-immunostaining of pMLC and PatJ reveals that they
1108 tend to accumulate on different junctions. Note junctions where Myosin accumulation
1109 predominates (arrows), and junctions where Crumbs2 predominates (arrowheads).
1110 Corresponding scatter plot shows more spread distribution and no correlation. **(C)**
1111 Immunostaining for ppMLC simultaneously revealed by two distinct secondary antibodies (Alexa
1112 488 and 647) as positive control, and corresponding scatter plot showing strong junctional
1113 intensity correlation after membrane segmentation. **(D)** Scatter plots showing the correlation of
1114 intensity of other pairs of proteins. **(E)** Correlation coefficients associated with scatter plots
1115 shown in A,B,C,D and Figure 5. Error bars represent s.e.m.
1116

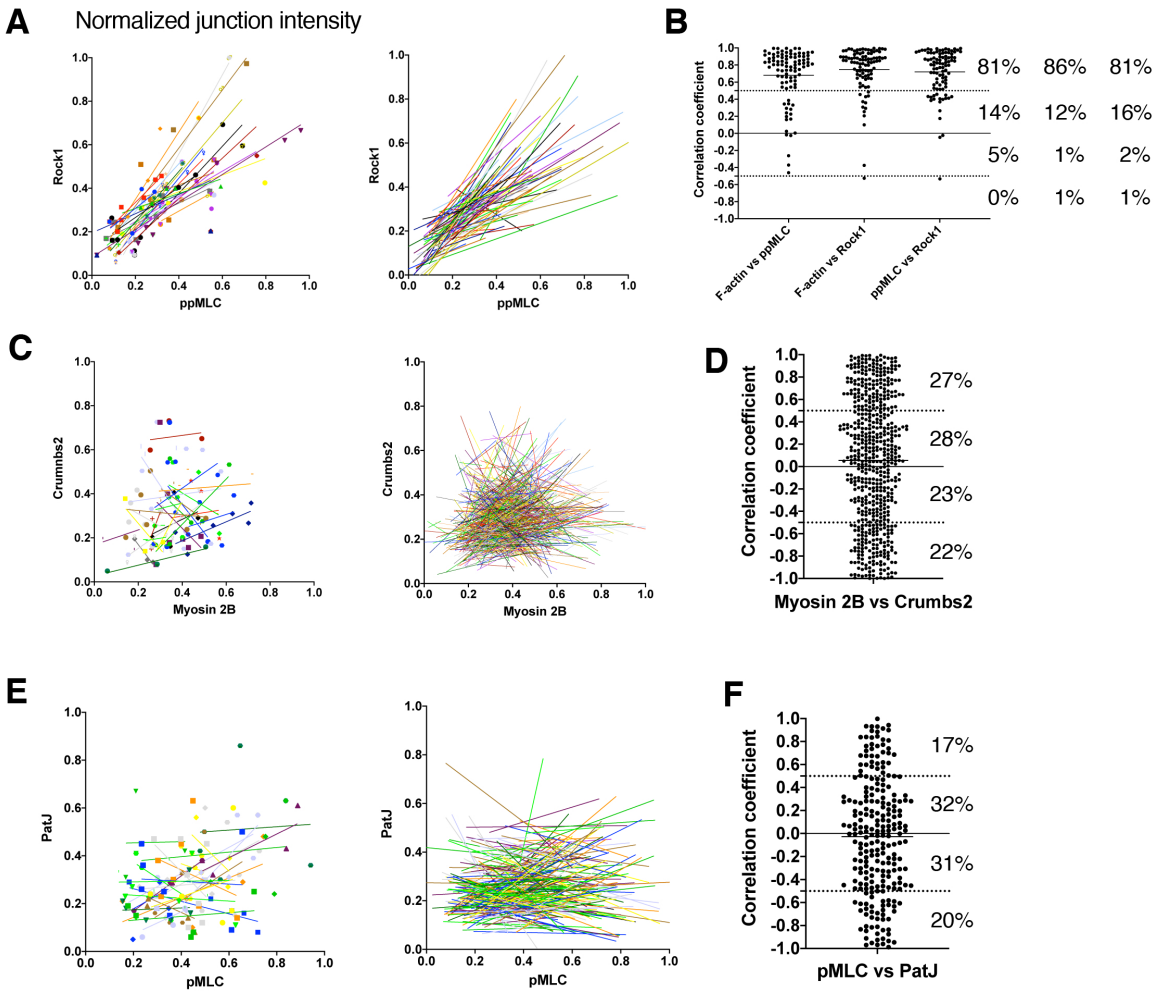

Figure 5-figure supplement 2: Junctional correlation of proteins at the single cell level. **(A)** Example of scatter plot showing the junctional intensity correlation of ppMLC and Rock1 in a cohort of cells. Each symbol represents one junction, grouped by cells (color coded) with respective correlation trends. Plot on the right shows only the correlation trend for a larger number of cells. **(B)** Correlation coefficients of ppMLC and Rock1 from plot shown in A, as well as F-actin and ppMLC, and F-actin and Rock1. Each dot represents the coefficient of correlation of junctions intensity of a single cell. % show the distribution of correlation coefficients in the different quarters. **(C)** Example of junctional intensity correlation of single cells for Crumbs2 and Myosin2B, depicting a mix of cells with correlation, some with no correlation, and some with anti-correlation. **(D)** Correlation coefficients reflecting the scatter plot shown in C, showing a broad distribution, from correlation (+1) to anti-correlation (-1). % show the distribution of correlation coefficients. **(E)** Example of junctional intensity correlation of single cells for PatJ and pMLC, depicting a mix of cells with correlation, some with no correlation, and some with anti-correlation. **(F)** Correlation coefficients reflecting the scatter plot shown in C, showing a broad

distribution, from correlation (+1) to anti-correlation (-1). % show the distribution of correlation coefficients.

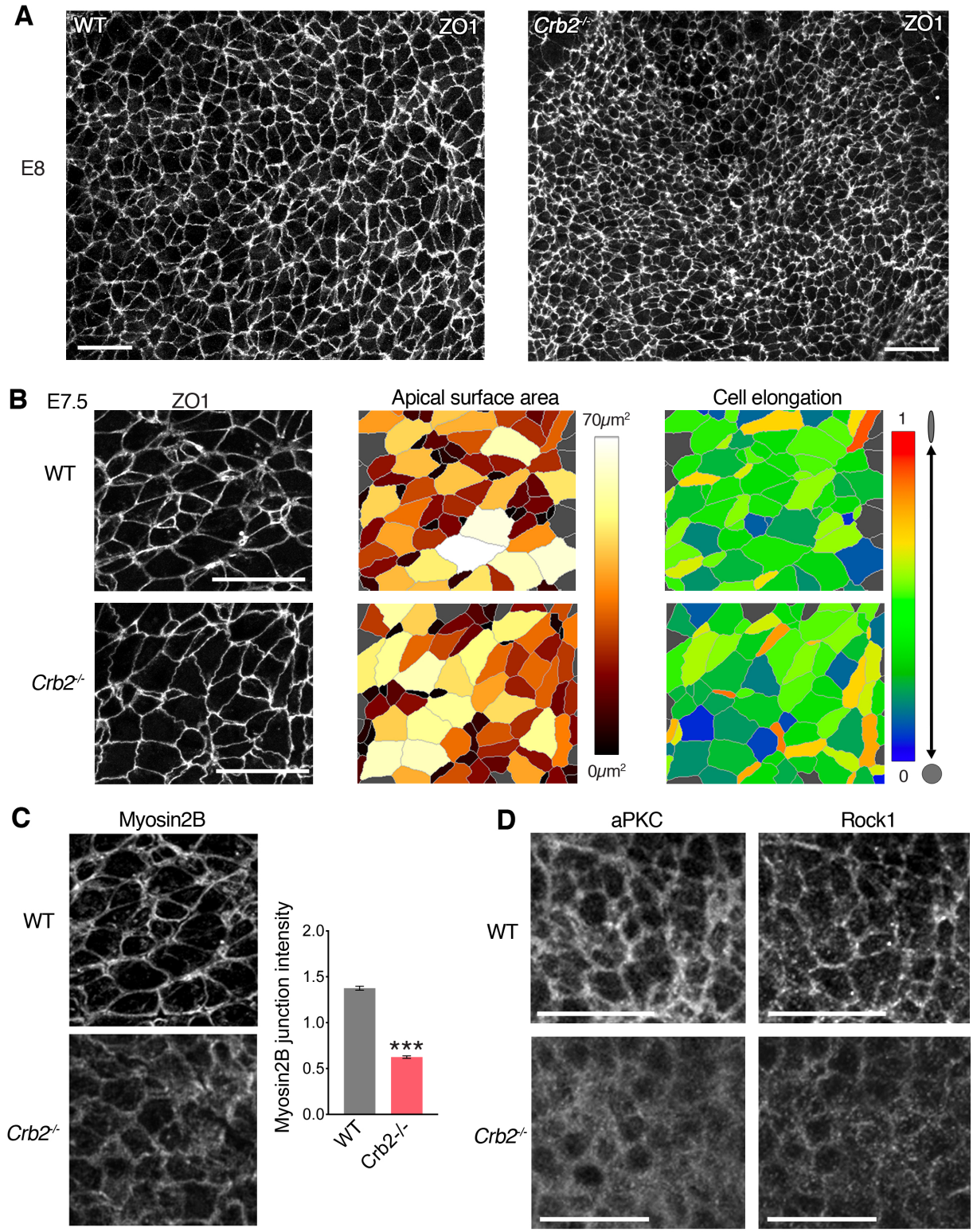

1135

1136 **Figure 6,7-figure supplement 1**: Cellular and molecular defects in *Crumbs2* mutant embryos.

1137 **(A)** Low magnification of ZO-1 staining show in the posterior epiblast in WT and *Crumbs2*

1138 mutants at E8.0. **(B)** ZO-1 immunostaining showing the apical surface of WT and *Crumbs2*

1139 mutant embryos at E7.5. Segmentation and color code of apical surface areas and surface
1140 elongation reveal normal size and shape of apical surface area in *Crumbs2* mutants at E7.5. **(C)**
1141 Immunostaining for Myosin2B at E7.5, showing reduced intensity in *Crumbs2* mutant embryos
1142 compared to WT. Graph shows significantly reduced Myosin2B intensity at junctions. **(D)**
1143 Immunostaining for aPKC and Rock1 in WT and *Crumbs2* mutants at E7.5 (intensity
1144 quantifications shown in Figure 7C).
1145 ***P<0.001 (Unpaired bilateral Mann-Whitney test). Error bars represent s.e.m.
1146
1147
1148 **Video S1.** Time-lapse imaging of a membrane-GFP reporter (recombined *mT/mG*)
1149 expressing embryo at embryonic day E7.5, showing apical constriction (right panel)
1150 associated to ingression, as cells move out of the epiblast epithelial layer basally to join
1151 the underlying mesoderm (left panel). Images were denoised and deconvolved, and
1152 represent single planes of optical sections and apical cell surfaces. The time-lapse
1153 spans 70min with 10min interval between frames.
1154
1155 **Video S2**. Time-lapse imaging of the posterior of a ZO-1-GFP reporter expressing
1156 embryo in the vicinity of the primitive streak at embryonic day E7.5. Tracking of
1157 individual cells reveals lateral epiblast cells converging toward the midline prior to their
1158 ingression. Cells around the midline (middle row) do not exhibit extensive movement in
1159 the plane of the epithelium. Movie of 240min with 5min interval between frames.
1160
1161 **Video S3**. Time-lapse of ZO-1-GFP showing rearrangement of cells in the epiblast near
1162 the primitive streak (top panel, 125min), and cell apical constriction and ingression away
1163 from the primitive streak, as the epiblast flows (to the left side) toward the midline
1164 (bottom panel, 55min). 5min interval between frames.
1165
1166 **Video S4**. Time-lapse of ZO-1-GFP highlighting 3 cells apically constricting and
1167 ingressing in the primitive streak region. 60min total with 5min interval between frames.
1168
1169 **Video S5**. Time-lapse of ZO-1-GFP highlighting a single cell at the primitive streak
1170 apically constricting. Membrane segmentation is performed over time such that different

1171 parameters can be followed and quantified, including the apical surface area, a cell's
1172 elongation and orientation, and the number of junctions. 95min total with 5min interval
1173 between frames.
1174
1175 **Video S6**. Segmentation of time-lapse showing color-code of cell apical surface (left
1176 panel), constriction rate (middle panel) and junction length (right panel) of a cell A
1177 shown in Figure 2. 40min total with 5min interval between frames.
1178
1179 **Video S7.** Time-lapse of ZO-1-GFP showing a cell cluster at the primitive streak. Most
1180 of the cells gradually constrict and ingress, and cells tracked after segmentation and
1181 color-coded for apical surface area and changes in surface area. Images were denoised
1182 and deconvolved. 115min with 5min interval between frames.
1183